Vibrational Modelling with an anHarmonic Oscillator Model in DSMC

Clément Civrais*, Craig White† and René Steijl‡
University of Glasgow, School of Engineering, James Watt South Building, G12 8QQ, Glasgow, United Kingdom

Vehicles undergoing hypersonic speed experience extreme aerothermodynamic conditions. Real gas effects cannot be neglected and thus internal degrees of freedom of molecules being partially/fully excited must be carefully predicted in order to accurately capture the physics of the flow-field. Within direct simulation Monte Carlo solvers, a harmonic oscillator (HO) model, where the quantum levels are evenly spaced, is typically used for vibrational energy. A more realistic model is an anharmonic oscillator (aHO), in which the energy between quantum levels is not evenly spaced. In this work, the Morse-aHO model is compared against HO. The Morse-aHO model is implemented in the *dsmcFoam+* solver and the numerical results are in excellent agreement with analytical and Potential Energy Surface solutions for the partition function, mean vibrational energy, and degrees of freedom. A method for measuring the vibrational temperature of the gas when using the anharmonic model in a DSMC solver is presented, which is essential for returning macroscopic fields. For important thermophysical properties of molecular oxygen, such as the specific heat capacity, it is shown that the aHO and HO models begin to diverge at temperatures above 1000 K, making the use of HO questionable for all but low enthalpy flows. For the same gas, including the electronic energy mode significantly improves the accuracy of the specific heat prediction, compared to experimental data, for temperatures above 2000 K. For relaxation from a state of thermal non-equilibrium, it is shown that the aHO model results in a slightly lower equilibrium temperature. When applied to hypersonic flow over a cylinder, the aHO model results in a smaller shock stand off distance and lower peak temperatures.

I. Introduction

Space exploration is one of the most demanding technological challenges. One of the major difficulty remains the entry into a planetary atmosphere where the space vehicle experiences large aerothermodynamic loading. Vehicles travelling at hypersonic velocities induce the formation of strong shock waves, behind which very high temperatures

*PhD Student, Aerospace Sciences Division, clement.civrais@glasgow.ac.uk - Corresponding author
†Senior Lecturer, Aerospace Sciences Division, craig.white.2@glasgow.ac.uk
‡Senior Lecturer, Aerospace Sciences Division, rene.steijl@glasgow.ac.uk

are created, with the result that real gas effects on the thermophysical properties of the flow cannot be neglected [1]. The number of degrees of freedom of the problem increases: in addition to the translational and rotational modes, one must take into account the vibrational and electronic modes [2]. Being closely related to the thermophysical properties through the partition functions, the degrees of freedom of a molecule must be carefully modelled to correctly capture the physics of the flow [2, 3].

One of the most popular manners to characterise the vibrational excitation of a diatomic molecular system is the simple harmonic oscillator (HO) model [2, 3], Eq. (1). Vibrational energies, ϵ_v, are equally-spaced over vibrational quantum levels, i, by a increment $h\nu$,

$$\epsilon_v^{HO}(i) = h\nu(i + \frac{1}{2}), \tag{1}$$

where ν is the fundamental frequency and h is Planck's constant.

Typically, the vibrational energy is re-scaled such that the ground state level has zero energy, which is permissible since it simply a constant and does not influence the changes of state of a system [1, 2, 4, 5]. In the HO model, the energy associated with a given quantum level can then be defined in terms of a characteristic vibrational temperature, Eq. (2),

$$\epsilon_v^{HO}(i) = ik\theta_v, \tag{2}$$

where k is the Boltzmann constant and θ_v is the characteristic vibrational temperature.

This model is often used in the direct simulation Monte Carlo (DSMC) community to address the vibrational excitation of molecular systems [6–8]. For reasonably low temperatures, where the flow is mainly governed by translational and rotational modes, the assumption of a molecular system acting as a HO is valid, whereas at high temperature, where the vibrational modes become significantly excited, the HO model meets its limitations [9–11]. As a result of the linear distribution of the vibrational energy over quantum levels, the modelling of the vibrational partition function, Q_v, is inaccurate at high temperature. Poorly modelling the partition function is undesirable because it is closely related to the thermophysical properties, e.g. the specific heat capacity of the gas $C_v(T)$,

$$C_v(T) = \frac{\partial^2}{\partial T^2}[Q^{trans}(T) + Q^{rot}(T) + Q^{vib}(T) + Q^{elec}(T)], \tag{3}$$

where Q is the partition function and the superscripts $()^{trans}$, $()^{rot}$, $()^{vib}$, and $()^{elec}$ refer to the translational, rotational, vibrational, and electronic modes, respectively, and T is the temperature. A failure to recover the correct thermophysical properties will lead to the physics of the flow not being captured accurately.

An alternative to avoid using a HO model for the description of vibrational excitation is to assume the molecular system to be an anharmonic oscillator (aHO) [2, 12, 13]. Instead of linearly relating vibrational energy and quantum levels, this model offers a non-equally spaced quantum level distribution, i.e. it assumes that the spacing between

quantum levels decreases with increasing energy. Describing the physical interaction that a molecule experiences with a non-linear approach significantly impacts the macroscopic properties of the physics of the flow [9–11].

Similar to an HO model, an aHO model is derived from a system composed of the time-independent Schrödinger equation and a potential energy function that describes the inter-atomic forces acting within the molecule [14–16]. In the HO framework, the potential function is derived from a simple quadratic formulation, while a large number of potential functions – and their corrected versions – can result in an aHO-like model, see Roy [17] for an extensive discussion around potential energy functions. Two of the most common functions that lead to an aHO-like model with application in DSMC are summarised in Table 1.

Table 1 Potential energy functions. S_k is the bond stiffness, c is the speed of light in vacuum, $\xi = \frac{r-r_{eq}}{r_{eq}}$ is the normalised distance between the nuclei, r_{eq} is the distance between the nuclei at the equilibrium state, a_0 and a_i are spectroscopic constants, α is a constant controlling the width of the potential, and D is the dissociation energy.

Name	Formulation
Harmonic Oscillator [2]	$V(\xi) = \frac{S_k r_{eq}^2}{2}\xi^2$
Dunham Expansion [13]	$V(\xi) = hca_0\xi^2(1 + \sum_i a_i\xi^i)$
Morse Potential [12]	$V(\xi) = D(1 - e^{-\alpha r_{eq}\xi})^2$

The Dunham expansion function makes use of a series expansion at an equilibrium molecular state. This model is widely used in spectroscopic and plasma research due to its ability to propose a simple coupling between the rotational, vibrational, and electronic modes of the molecular system [18–20].

Anharmonic oscillator models have been employed in the past to address the vibrational excitation in DSMC simulations [21–25] and in CFD simulations [9, 26–28]. The Morse-aHO model has previously been used in DSMC simulations. It was applied as the foundation for Koura's studies [23, 29, 30] on the rotational relaxation of diatomic species. Similarly, Haas [21] employed the Morse-aHO model to propose a new model for reactive collisions in order to capture coupled vibration-dissociation (CVD) mechanisms prevalent in high-temperature rarefied gases [31–33]. The authors show that the Morse-aHO model indicates the best agreement to empirical data when compared to the other vibrational models considered. The coupling between vibrational excitation and the dissociation phenomena is a field of active research [34–36], showing the benefits of modelling the vibrational excitation with an aHO model. Bird also implemented the Morse-aHO model in his code to include anharmonic vibrational energy levels in a test case in his 1994 monograph [4], where the impact of this on dissociation rates was studied. It was found that the measured dissociation rates were greater than that from the harmonic oscillator model, although some uncertainty remained over the selection procedure for post-collision vibrational energies being taken from a uniform distribution when the energies are not uniformly distributed.

However, to the best of the authors' knowledge, the details of how to implement an aHO model in a DSMC solver have not been explicitly described before. This article therefore aims to describe the implementation of such a model in

a DSMC solver and to study the influence of having an aHO rather than a HO model. The focus will be on the Morse potential [12] and Dunham expansion [13] for the computation of macroscopic and thermophysical properties of a diatomic gas.

As is evident from Eq. (3), the electronic mode must also be taken into account to return the correct macroscopic properties of a high temperature gas [4]. At low temperatures, the flow is mainly governed by the translational and rotational modes, whereas at high temperatures, the contributions of vibrational and electronic modes are no longer negligible and play a major role in the correct representation of the physics of the flow. The electronic mode has sometimes been omitted in DSMC studies [37] due to its strong connection to ionisation and plasma simulations; this decision is surprising while dealing with Mach numbers in excess of 30 and temperatures of almost 20,000 K [37]. The consequences of such an omission on the thermophysical properties will also be investigated in the current work.

The aims of this work are threefold. The key contribution of the current article is on the quantification of the influence of modelling the vibration excitation with either a traditional HO model or a Morse-aHO model on the thermophysical properties. Although aHO-type models have been employed in DSMC before [21–25], none of the articles detail how it has been implemented and the necessary modifications required in the DSMC solver. Therefore, the development of a aHO model compatible with the DSMC principle, as well as a novel technique for measuring the vibrational temperature of the gas when an aHO model is used, will be addressed. Moreover, electronic mode omission is a questionable assumption for the recovery of the thermophysical properties of a gas for all but low enthalpy flows and the impact of this will be investigated. To summarise, the novelty of the article lies in the development of a Morse-aHO model, validated against well-established test cases and high-accuracy data, and its application to different problems.

The rest of the article is organized as follows: in Sec. II, the derivation of two aHO models, namely Dunham expansion and Morse potential, are presented. The important characteristics of these models are regarded in terms of the physical description of the dissociation phenomena. The implementation of the Morse-aHO model in the *dsmcFoam+* [38] solver is detailed in a step-by-step fashion. In Sec. III, the Morse potential function is validated against theory and compared to the traditional HO model. In Sec. IV, the impact of the vibrational model and the omission of electronic mode on thermophysical properties of fundamental problems is studied. In Sec. V, the Morse aHO model is tested for a flow past a cylindrical body. The final section, Sec. VI, provides conclusions and perspectives for future work.

II. Vibrational Modelling Theory

The derivation of the vibrational energy, ϵ_v, is a matter of solving the time-independent Schrödinger equation [14–16] for a chosen potential function [17], i.e. Morse potential [12], Dunham expansion [13], or any other potential function [17]. Obtaining the vibrational energy consists of applying a convenient coordinate transformation and evaluating the eigen-value of the system. The complete derivation from quantum mechanics of the HO model can be

found in Refs. [14, 15], for the Morse-aHO model in Refs [12, 14–16, 39], and for Dunham-aHO model in Ref [13].

A. Dunham Expansion

With Dunham theory, a diatomic molecule is modelled as a rotating vibrator [13] that has two contributions. The total potential is obtained by summing the rotational and vibrational contributions. Applying the relevant mathematical transformation [13, 13–16], the internal ro-vibrational energy has the form of a double infinite summation that accounts for each contribution,

$$\epsilon_{v,r}^{Dunham}(i,K) = hc \sum_{m} \sum_{n} Y_{m,n}(i+\frac{1}{2})^m [f(K)]^n, \tag{4}$$

where $Y_{m,n}$ is related to a spectroscopy constant [13], i is the vibrational quantum level, $f(K)$ a function that accounts for the calculation of the rotational energies.

In the context of uncoupling internal modes and targeting the vibrational excitation of a diatomic molecule, the n^{th} summation, referring to rotational motion, can be dropped to zero. Due to the infinite nature of the summation over m, this function must be arbitrarily truncated to a certain level. This decision is mainly governed by the availability of spectroscopy constants [40–42] for the computation of the weighted parameter $Y_{m,n}$. These coefficients are tabulated in Refs. [40, 42] for a selection of chemical species. Developing Eq. (4) up to the third order results in a commonly used expression [18, 19];

$$\epsilon_{v}^{Dunham}(i) = hc\omega_e(i+\frac{1}{2})(1-\chi_e(i+\frac{1}{2})+\gamma_e(i+\frac{1}{2})^2), \tag{5}$$

where ω_e, $\omega_e\chi_e$ and $\omega_e\gamma_e$ are spectroscopy constants.

B. Morse Potential

Similarly, the Morse potential [12] defines the vibrational energies as the eigen-value of the system composed of the time-independent Schrödinger equation and the Morse potential [12].

The vibrational energy is readily obtained by applying the appropriate transformation and extracting the eigen-value of the system,

$$\epsilon_{v}^{Morse}(i) = h\nu(i+\frac{1}{2}) - \frac{[h\nu(i+\frac{1}{2})]^2}{4D}, \tag{6}$$

where D is the dissociation energy and ν is the fundamental frequency, defined as

$$\nu = \frac{\alpha}{2\pi}\sqrt{\frac{D}{m}}, \tag{7}$$

where the parameter α controls the width of the potential function and m is the mass.

The first term on the right hand side of Eq. (6) is equivalent to the HO model and the second, negative, term is responsible for the change from the parabolic shape to an asymptotic behavior towards the dissociation limit.

C. Comparison

To compare the previously described models at an equivalent level, it is necessary to follow the same convention. For this purpose, the vibrational energy derived through a Morse Potential can be re-written in the form of a function that accounts for spectroscopy constants only. The most popular sources for obtaining these constants are the National Institute of Standards and Technology (NIST) database [43] or the Huber and Herzberg tables [40, 41]. However, as has previously been noted by other authors [28], the use of these constants often over-estimates the number of vibrational quantum levels and the dissociation energy of a molecule [44]. Therefore, the spectroscopic constants used in this work have been fitted to high-accuracy Potential Energy Surface (PES) data [45]. Table 2 presents the fitted spectroscopy constants along with the values extracted from the Huber and Herzberg tables [40, 41] for three molecular systems lying at the ground state level.

Table 2 Spectroscopy constants for three ground state diatomic molecules.

Species	ω_e (cm^{-1}) [41]	Fitted $\omega_e(cm^{-1})$	$\omega_e\chi_e$ (cm^{-1}) [41]	Fitted $\omega_e\chi_e$ (cm^{-1})	D (eV) [41]
N_2 $(X^1\ \sum_g^+)$	2358.57	2345.99	14.324	17.454	9.759
O_2 $(X^3\ \sum_g^-)$	1580.19	1671.74	11.981	16.425	5.116
NO $(X^2\ \Pi_r)$	1904.20	1949.98	14.075	17.305	6.497

For Eq. (6) to be expressed in terms of the spectroscopic constants from Tab. 2, the first step is to express both the fundamental frequency, Eq. (7), and dissociation energy in terms of spectroscopy constants [5, 28], i.e.,

$$\nu = c\omega_e, \tag{8}$$

and,

$$D = hc\frac{\omega_e^2}{4\omega_e\chi_e}. \tag{9}$$

Substituting Eqs. (8)-(9) in Eq. (6), the Morse-vibrational energy can now be written as:

$$\epsilon_v^{Morse}(i) = hc\omega_e(i+\frac{1}{2}) - hc\omega_e\chi_e(i+\frac{1}{2})^2. \tag{10}$$

As previously mentioned, for the calculation of thermophysical flow properties, the zero-point energy is subtracted in the calculation of the vibrational energy [1, 4, 10, 11, 46, 47]. Note that this treatment is also applied to the translational and electronic modes as mentioned in Refs. [1, 4, 46, 47]. Therefore, Eq. (10) can be reduced to the following expression,

$$\epsilon_v^{Morse}(i) = \epsilon_v^{Morse}(i) - \epsilon_v^{Morse}(0) = hc\omega_e i - hc\omega_e\chi_e(i^2+i). \tag{11}$$

The result of this is illustrated in Fig. 1, where aHO models, i.e. the Dunham and Morse, are compared to the HO

model for the calculation of the vibrational energy for the nitrogen molecule lying at ground state level. The vibrational energies are calculated with both sets of spectroscopic constants shown in Tab. 2. The calculation of the vibrational energy with the Huber and Herzberg table values [40] are denoted by $H.\ and\ H.$. The calculation of the vibrational energy with the values fitted to PES calculations are denoted by $Fitted$ and the dissociation limit is denoted by D. The vibrational energies of the three diatomic molecules summarised in Table 2 are tabulated in Tables 3, 4 and 5 for N_2, O_2, and NO, respectively.

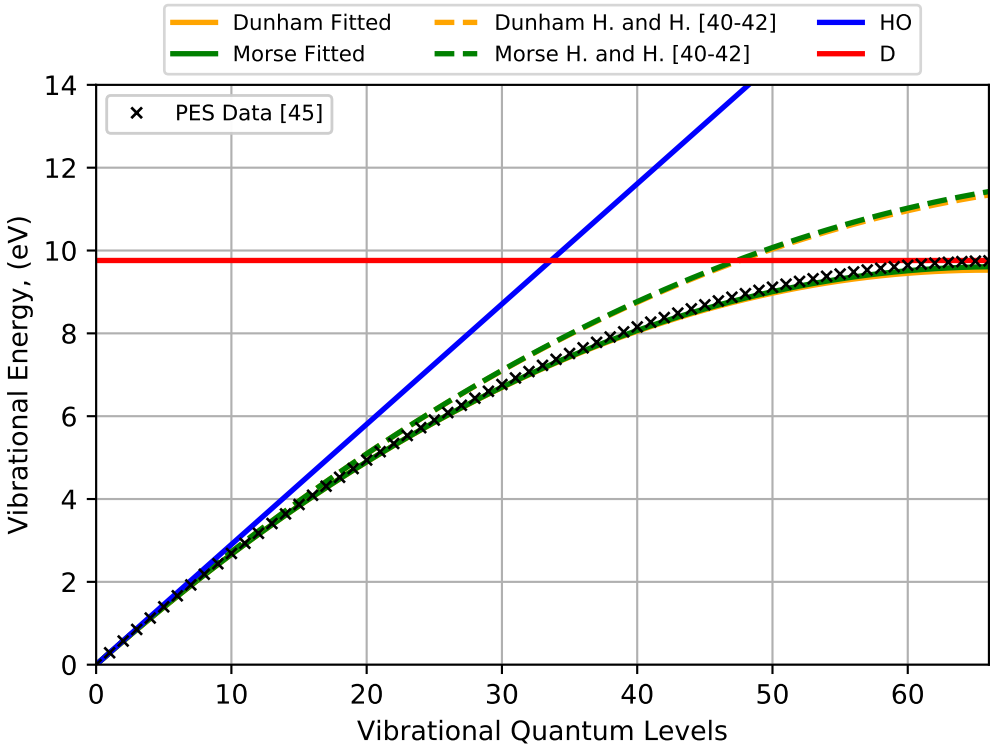

Fig. 1 Vibrational energy for molecular nitrogen at the ground state level.

In the preamble of this manuscript, the foundation of the HO model has been detailed. This vibrational model is based on an equally spaced representation of the vibration quantum levels which, in turn, leads to a linear behavior of the vibrational energy, as clearly illustrated in Fig. 1. In aHO models, the spacing between levels is no longer uniformly distributed. In fact, the latter possesses a second order negative term that decreases the gap between levels as the level increases. This pattern is particularly noticeable in Fig. 1, with a high concentration of energy in the high-lying vibrational quantum levels.

Note that the vibrational energies computed with the Huber and Herzberg tables [40] match the PES data [45] for the first 14 vibrational quantum levels of molecular nitrogen. Beyond this, the vibrational energies diverge as the energy levels increase. It is clear that these spectroscopic constants over-estimate the vibrational energy and allow it to obtain values significantly above the accepted dissociation energy, as previously noted by Da Silva [28].

Table 3 Vibrational energy for Nitrogen molecular at ground state.

i	$\epsilon_v^{HO}(i),\ eV$	$\epsilon_v^{Morse}(i),\ eV$	$\epsilon_v^{Dunham}(i),\ eV$	$\epsilon_v^{PES}(i),\ eV$ [45]
0	0.0000	0.0000	0.0000	0.0000
1	0.2903	0.2860	0.2859	0.2881
2	0.5805	0.5676	0.5676	0.5719
3	0.8708	0.8449	0.8449	0.8513
4	1.1611	1.1179	1.1179	1.1265
5	1.4513	1.3866	1.3865	1.3973
6	1.7416	1.6509	1.6508	1.6638
7	2.0319	1.9110	1.9108	1.9260
8	2.3222	2.1667	2.1665	2.1839
9	2.6124	2.4181	2.4178	2.4375
10	2.9027	2.6652	2.6648	2.6867
11	3.1930	2.9079	2.9075	2.9316
12	3.4832	3.1464	3.1458	3.1722
13	3.7735	3.3805	3.3798	3.4085
14	4.0638	3.6103	3.6094	3.6405
15	4.3540	3.8358	3.8347	3.8681
16	4.6443	4.0569	4.0557	4.0914
17	4.9346	4.2738	4.2723	4.3104
18	5.2249	4.4863	4.4845	4.5251
19	5.5151	4.6945	4.6924	4.7355
20	5.8054	4.8984	4.8960	4.9416
21	6.0957	5.0980	5.0952	5.1433
22	6.3859	5.2932	5.2900	5.3407
23	6.6762	5.4842	5.4805	5.5338
24	6.9665	5.6708	5.6667	5.7226
25	7.2567	5.8531	5.8484	5.9070
26	7.5470	6.0310	6.0258	6.0872
27	7.8373	6.2047	6.1989	6.2630
28	8.1276	6.3740	6.3676	6.4345
29	8.4178	6.5390	6.5319	6.6017
30	8.7081	6.6997	6.6918	6.7645
31	8.9984	6.8561	6.8474	6.9231
32	9.2886	7.0082	6.9986	7.0773
33	9.5789	7.1559	7.1454	7.2272
34	9.8692	7.2993	7.2879	7.3728
35	10.1594	7.4384	7.4259	7.5140
36	10.4497	7.5732	7.5596	7.6510
37	10.7400	7.7037	7.6889	7.7836
38	11.0303	7.8298	7.8139	7.9119
39	11.3205	7.9517	7.9344	8.0359
40	11.6108	8.0692	8.0506	8.1556
41	11.9011	8.1824	8.1624	8.2709
42	12.1913	8.2912	8.2698	8.3820
43	12.4816	8.3958	8.3728	8.4887
44	12.7719	8.4960	8.4714	8.5911
45	13.0621	8.5919	8.5656	8.6891
46	13.3524	8.6835	8.6554	8.7829
47	13.6427	8.7708	8.7408	8.8723
48	13.9330	8.8538	8.8219	8.9575
49	14.2232	8.9324	8.8985	9.0383
50	14.5135	9.0067	8.9707	9.1147
51	14.8038	9.0767	9.0385	9.1869
52	15.0940	9.1424	9.1019	9.2547
53	15.3843	9.2037	9.1609	9.3182
54	15.6746	9.2608	9.2155	9.3774
55	15.9648	9.3135	9.2657	9.4323
56	16.2551	9.3619	9.3115	9.4829
57	16.5454	9.4060	9.3528	9.5291
58	16.8357	9.4458	9.3898	9.5710
59	17.1259	9.4812	9.4223	9.6086
60	17.4162	9.5123	9.4504	9.6419
61	17.7065	9.5391	9.4741	9.6709
62	17.9967	9.5616	9.4934	9.6955
63	18.2870	9.5798	9.5082	9.7158
64	18.4060	9.5937	9.5186	9.7318
65	18.6936	9.6032	9.5246	9.7435
66	18.9812	9.6084	10.1920	9.7508

Table 4 Vibrational energy for Oxygen molecular at ground state.

i	$\epsilon_v^{HO}(i),\ eV$	$\epsilon_v^{Morse}(i),\ eV$	$\epsilon_v^{Dunham}(i),\ eV$	$\epsilon_v^{PES}(i),\ eV$ [45]
0	0.0000	0.0000	0.0000	0.0000
1	0.2068	0.2028	0.2028	0.1932
2	0.4137	0.4015	0.4015	0.3838
3	0.6205	0.5961	0.5961	0.5720
4	0.8274	0.7867	0.7867	0.7575
5	1.0342	0.9733	0.9732	0.9404
6	1.2411	1.1557	1.1555	1.1205
7	1.4479	1.3341	1.3339	1.2978
8	1.6548	1.5084	1.5081	1.4722
9	1.8616	1.6787	1.6782	1.6436
10	2.0684	1.8449	1.8442	1.8119
11	2.2753	2.0070	2.0061	1.9772
12	2.4821	2.1651	2.1639	2.1393
13	2.6890	2.3191	2.3177	2.2981
14	2.8958	2.4690	2.4673	2.4536
15	3.1027	2.6149	2.6127	2.6057
16	3.3095	2.7567	2.7541	2.7543
17	3.5163	2.8945	2.8913	2.8993
18	3.7232	3.0282	3.0244	3.0407
19	3.9300	3.1578	3.1534	3.1784
20	4.1369	3.2833	3.2783	3.3123
21	4.3437	3.4048	3.3990	3.4424
22	4.5506	3.5222	3.5156	3.5684
23	4.7574	3.6356	3.6280	3.6904
24	4.9643	3.7449	3.7363	3.8082
25	5.1711	3.8501	3.8404	3.9218
26	5.3779	3.9513	3.9404	4.0311
27	5.5848	4.0484	4.0362	4.1359
28	5.7916	4.1414	4.1278	4.2362
29	5.9985	4.2304	4.2153	4.3318
30	6.2053	4.3153	4.2987	4.4226
31	6.4122	4.3962	4.3778	4.5085
32	6.6190	4.4729	4.4528	4.5893
33	6.8259	4.5457	4.5236	4.6649
34	7.0327	4.6143	4.5902	4.7353
35	7.2395	4.6789	4.6526	4.8001
36	7.4464	4.7394	4.7109	4.8592
37	7.6532	4.7959	4.7649	4.9125
38	7.8601	4.8483	4.8147	4.9598
39	8.0669	4.8966	4.8604	5.0009
40	8.2738	4.9409	4.9018	5.0355
41	8.4806	4.9811	4.9391	5.0635
42	8.6875	5.0172	4.9721	5.0850
43	8.8943	5.0493	5.0009	5.0999
44	9.1011	5.0773	5.0255	5.1089
45	9.3080	5.1012	5.0459	5.1134
46	9.5148	5.1211	5.0620	5.1150

The change from linear to non-linear behavior directly influences the quantum level reached at the dissociation energy. For a nitrogen molecule under the HO assumption, the dissociation limit is reached for a quantum level of 33, while under the Morse-aHO assumption, the dissociation occurs at quantum level 47 for the the vibrational energies computed with the Huber and Herzberg tables [40], or 66 for the PES fitted vibrational energies. A delay in the dissociation of the molecule as indicated by Fig. 1 causes a noticeable change in the chemistry of the molecule. Although this fundamental aspect is of interest in the context of high speed flow simulations, chemical reaction rates are not investigated in the current work.

Table 5 Vibrational energy for Nitric Oxide molecular at ground state.

i	$\epsilon_v^{HO}(i),\ eV$	$\epsilon_v^{Morse}(i),\ eV$	$\epsilon_v^{Dunham}(i),\ eV$	$\epsilon_v^{PES}(i),\ eV$ [45]
0	0.0000	0.0000	0.0000	0.0000
1	0.2413	0.2370	0.2370	0.2289
2	0.4825	0.4697	0.4697	0.4548
3	0.7238	0.6981	0.6981	0.6778
4	0.9651	0.9223	0.9221	0.8977
5	1.2064	1.1421	1.1419	1.1145
6	1.4476	1.3577	1.3573	1.3281
7	1.6889	1.5690	1.5684	1.5385
8	1.9302	1.7760	1.7752	1.7457
9	2.1714	1.9787	1.9776	1.9495
10	2.4127	2.1772	2.1756	2.1499
11	2.6540	2.3714	2.3693	2.3469
12	2.8952	2.5612	2.5586	2.5404
13	3.1365	2.7468	2.7435	2.7303
14	3.3778	2.9282	2.9240	2.9166
15	3.6191	3.1052	3.1001	3.0993
16	3.8603	3.2779	3.2718	3.2781
17	4.1016	3.4464	3.4391	3.4532
18	4.3429	3.6106	3.6020	3.6244
19	4.5841	3.7705	3.7604	3.7917
20	4.8254	3.9261	3.9144	3.9550
21	5.0667	4.0775	4.0640	4.1142
22	5.3080	4.2246	4.2091	4.2692
23	5.5492	4.3673	4.3497	4.4200
24	5.7905	4.5058	4.4858	4.5665
25	6.0318	4.6401	4.6175	4.7087
26	6.2730	4.7700	4.7447	4.8464
27	6.5143	4.8956	4.8673	4.9795
28	6.7556	5.0170	4.9855	5.1080
29	6.9968	5.1341	5.0992	5.2318
30	7.2381	5.2469	5.2083	5.3508
31	7.4794	5.3554	5.3129	5.4648
32	7.7207	5.4597	5.4129	5.5738
33	7.9619	5.5596	5.5084	5.6777
34	8.2032	5.6553	5.5994	5.7763
35	8.4445	5.7467	5.6858	5.8695
36	8.6857	5.8338	5.7676	5.9572
37	8.9270	5.9166	5.8449	6.0392
38	9.1683	5.9952	5.9175	6.1153
39	9.4095	6.0694	5.9856	6.1855
40	9.6508	6.1394	6.0490	6.2495
41	9.8921	6.2051	6.1078	6.3072
42	10.1334	6.2665	6.1621	6.3582
43	10.3746	6.3237	6.2116	6.4024
44	10.6159	6.3765	6.2566	6.4394
45	10.8572	6.4251	6.2969	6.4690
46	11.0984	6.4694	6.3326	6.4909
47	11.3397	6.5094	6.3635	6.5045

Another outcome highlighted in Fig. 1 is the validity of the HO assumption. It is perceptible that, due to the linear behavior, the HO model is an acceptable hypothesis in a configuration where only a small portion of vibrational levels are excited. In another words, HO fits for low enthalpy flows, but as the temperature increases, it should be replaced by an aHO model.

III. Implementation and Validation of Morse-aHO model

A. *dsmcFoam+* solver

Similar to MONACO [48], DAC [49], SPARTA [50], and others, *dsmcFoam+* is a DSMC solver developed around the foundation of the method established by Bird [4]. It is built within the OpenFOAM framework [51]. In the current work, a version of *dsmcFoam+* that is implemented within OpenFOAM-v2112 is used. A custom version of this solver, developed at the University of Glasgow, possesses vibrational and electronic energies [38]. In order to provide a more realistic description of the vibrational excitation of a diatomic molecule, the aHO model derived from the Morse potential, Sec. II, has been implemented in the *dsmcFoam+* solver. As described in detail previously, rather than computing the vibrational energy through the use of the characteristic vibrational temperature, aHO vibrational levels have been pre-calculated and inserted within the *dsmcFoam+* species definitions as an additional "look-up table" entry, in a similar fashion to the treatment of electronic energy [38].

The redistribution of internal energies is ensured by a serial application of the quantum Larsen-Borgnakke (LB) method [4, 52] using the HO model or the Morse-aHO model to compute the vibrational energy of the molecule. Various alternatives can be used to redistribute the internal energy with sophisticated approaches, i.e. forced harmonic oscillator [44, 53], Quasi-Classical Trajectory Calculation-DSMC [54, 55], Classical Trajectory Calculation-DSMC [23, 29] or a 'state-to-state' approach [22]. These techniques can provide a highly-accurate description of the quantum transitions for the distribution of the energy toward various internal energetic channels, i.e. vibrational-translational (VT) [22, 53, 56], vibrational-vibrational (VV) [22, 53, 56], or vibrational-vibrational-translational (VVT) [53] transitions. Although the state-to-state technique has a clear advantage in that it offers an almost complete description of energy transitions, which is the key difference between traditional LB and the cited models, this technique increases the level of complexity to keep track of the full transitions and the corresponding rates that a molecule can experience (single/multi-quantum jumps). In the current work, the choice has been made to keep the application of the quantum LB method to maintain a certain level of sophistication. The combination of the Morse-aHO model and LB can provide a significant improvement in the calculation of the macroscopic and thermophysical properties without adding significant complexity to the algorithms, or expense to the numerical simulations.

B. Implementation of Morse-aHO model in *dsmcFoam+*

The DSMC method [4] is a stochastic particle-based technique for obtaining a solution to the Boltzmann equation. In the framework of the method, internal energies are commonly redistributed through a serial application of the quantum Larsen-Borgnakke (LB) method [4, 52]. A general illustration of the serial application of the method to redistribute the energy through the internal modes is shown in Fig. 2.

The quantum Larsen-Borgnakke technique to redistribute the internal energy is a four-step procedure. The purpose of Step 1 (top left) and 3 (top right) is to allocate a portion of the collision energy to the vibrational modes of particles A and B, respectively. Similarly, Step 2 (bottom left) and 4 (bottom right) aim to redistribute the collision energy to the rotational mode of the collision partners.

Assuming all stages of the collision process are inelastic, the pre-collision energy of the collision partners A and B, E_C, is calculated as the sum of the relative translational energy of the pair A and B, ϵ_t, and the pre-collision vibrational energy of particle A, $\epsilon_{v,A}$,

$$E_{C,1} = \epsilon_t + \epsilon_{v,A}. \tag{12}$$

After this process, the collision energy is redistributed between a new translational energy, $\epsilon^*_{t,1}$ and the newly selected vibrational energy $\epsilon^*_{v,A}$ (where the superscript $()^*$ refers to post-collision properties), such that

$$\epsilon_{t,1} = E_{C,1} - \epsilon^*_{v,A}. \tag{13}$$

This procedure is then applied successively to the rotational mode of particle A and repeated for particle B.

Fig. 3 shows the general three-step procedure to assign the post-collision vibrational energy levels, whether an HO or aHO model is used. The first step is to test the particle for vibrational energy exchange and compute the maximum available post-collision vibrational quantum level, i^*_{max}. If an inelastic collision is accepted, a post-collision quantum level is uniformly chosen between 0 and i^*_{max}; if the particle is not accepted for energy exchange, the function returns the initial vibrational quantum level, i_p. Finally, an acceptance-rejection method is used to select a value of i^* from the distribution $\frac{P(E_C,i^*)}{P(E_C,i^*_{max})}$.

In the context of an anharmonic oscillator model, the implementation only slightly differs from the traditional harmonic oscillator model. When using the HO model, the vibrational energies for a diatomic molecule are supplied as a list that is a species property, similar to the electronic energy list [38]. Vibrational energies for N_2, O_2, and NO have been calculated and are provided in Tabs. 3, 4, and 5, respectively. For other diatomic species, vibrational energies can be calculated using Eq. (6) and Refs. [40–42]. In DSMC, it is good practice to avoid the utilisation of macroscopic temperature [4, 38, 58]; therefore the next step is to define a collision temperature, T_{coll}, when a pair are selected for

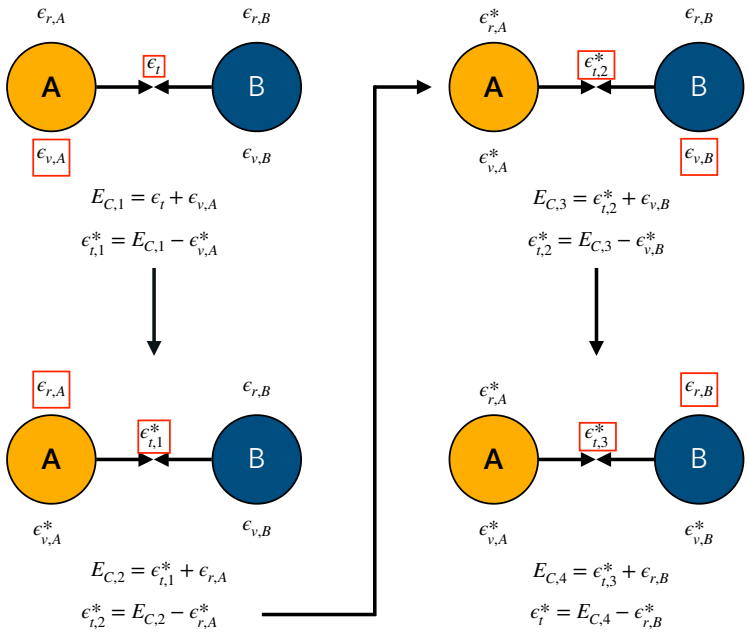

Fig. 2 Flowchart of the serial application of the quantum Larsen-Borgnakke techniques [52] (adapted from [57]).

collision,

$$T_{coll} = \frac{\epsilon_v(i^*_{max})}{k(7/2-\omega)} = \begin{cases} \frac{i^*_{max}\theta_v}{(7/2-\omega)} & \text{if HO model,} \\ \frac{hc\omega_e i^*_{max}(1-\chi_e(i^*_{max}+1))}{k(7/2-\omega)} & \text{if aHO model,} \end{cases} \tag{14}$$

where $\epsilon_v(i^*_{max})$ refers to the vibrational energy at quantum level i^*_{max}.

For the HO model, the maximum vibrational quantum level, i^*_{max}, is,

$$i^*_{max} = \left\lfloor \frac{E_C}{k\theta_v} \right\rfloor, \tag{15}$$

where ω is the viscosity index, E_C is the collision energy, which is the sum of the pre-collision vibrational energy for the particle under consideration and the relative translational energy, and i^*_{max} denotes the maximum vibrational quantum level available.

For the Morse-aHO model, the maximum vibrational quantum level is obtained by looping through the list of vibrational energies and finding the vibrational quantum level that satisfies the conditions of Eq. (16), i.e.

$$i^*_{max} = \begin{cases} \text{increment } i, & \text{if } E_C > \epsilon_v(i), \\ \text{accept } (i-1), & \text{if } E_C < \epsilon_v(i). \end{cases} \tag{16}$$

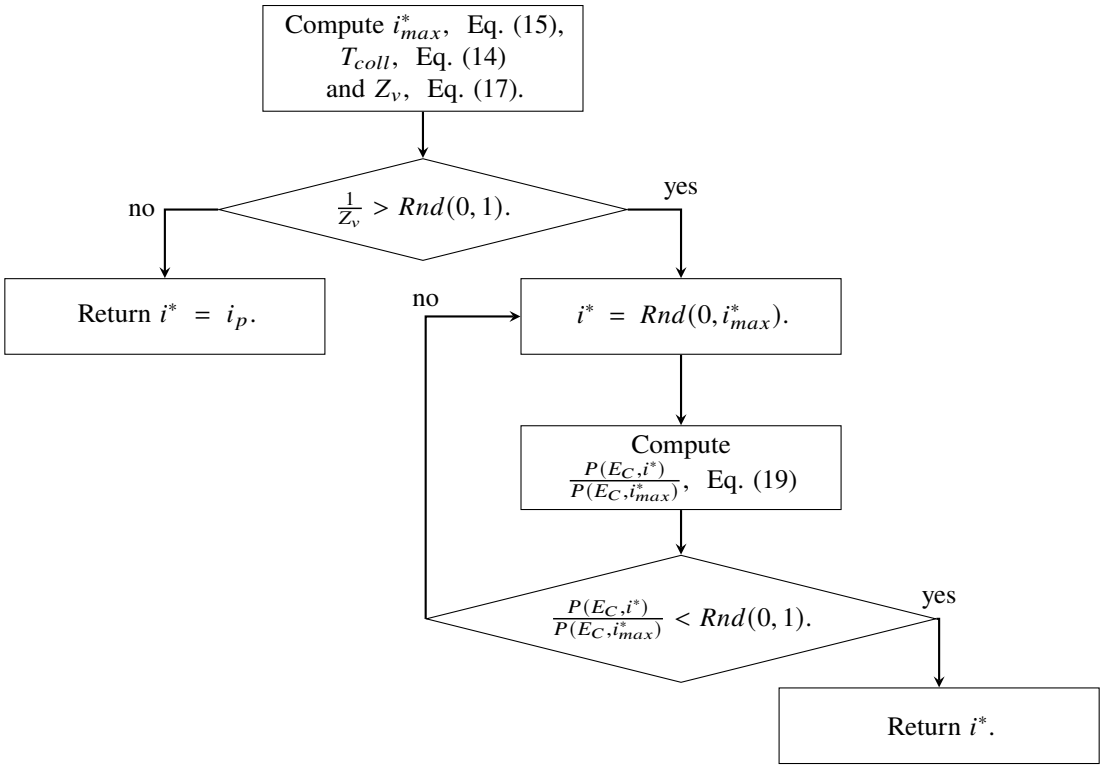

Fig. 3 Flowchart of the post-collision treatment of the vibrational energy levels.

The vibrational collision number, Z_v, is calculated from Eq. (17) [4, 58],

$$Z_v = \left(\frac{D}{T_{coll}}\right)^{\omega} \left[Z_{ref} \left(\frac{D}{T_{coll}}\right)^{-\omega} \right]^{\frac{\left(\frac{D}{T_{coll}}\right)^{1/3}-1}{\left(\frac{D}{T_{Z_{ref}}}\right)^{1/3}-1}}, \tag{17}$$

where Z_{ref} is the vibrational collision number at a reference temperature T_{ref},

$$Z_{ref} = \frac{C_1}{T_{ref}^{\omega}} e^{-C_2 T_{ref}^{\frac{1}{3}}}, \tag{18}$$

where the parameters C_1, C_2, and ω are given in Appendix A of Ref. [4].

If accepted for vibrational relaxation, the potential post-collision vibrational quantum level of the particle is uniformly chosen between $i = 0$ and the maximum possible level i^*_{max}. The acceptance-rejection method is applied to select a value of i^* from the probability ratio, Eq. (19),

$$\frac{P(E_C, i^*)}{P(E_C, i^*_{max})} = \begin{cases} \left(1 - \frac{i^* k \theta_v}{E_c}\right)^{3/2-\omega_{A,B}} & \text{if HO model.} \\ \left(1 - \frac{hc\omega_e i^*(1-\chi_e(i^*+1))}{E_c}\right)^{3/2-\omega_{A,B}} & \text{if aHO model.} \end{cases} \tag{19}$$

where $\omega_{A,B}$ is the average viscosity exponent of the collision pair A and B, see Fig. 2.

As shown above, the redistribution of internal energy is slightly modified by the inclusion of an aHO model. However, it is a relatively simple adaptation since the procedure is similar to the one typically used for electronic energy [59]. The main differences lie in the calculation of the maximum allowed vibrational quantum level, i^*_{max}, Eq. (16) and the probability calculation where the vibrational energies are calculated with Eq. (6) for the Morse-aHO model instead of Eq. (2) for the HO model.

C. Validation test case

Changing from a linear behaviour with an HO model to a non-linear behaviour implies a different response to an external excitation. It has been observed in Sec. II that due to the negative non-linear term, a larger proportion of the vibrational energy is concentrated in the high-lying vibrational quantum levels compared to the HO model. This has significant consequences on the high-lying vibrational quantum level population. Usually, these levels are populated through a Boltzmann distribution

$$f_i \equiv \frac{e^{\frac{-\epsilon_v(i)}{kT}}}{\sum_j e^{\frac{-\epsilon_v(j)}{kT}}}, \tag{20}$$

where ϵ_v is the energy in the i^{th} vibrational quantum level.

With the population density being a function of the internal vibrational energy, a change from a linear to a non-linear profile is expected. As it is the fundamental characteristic point of the aHO model, this quantity is selected as a validation test case for the implementation of Morse-aHO model within *dsmcFoam+* [38].

A 0-D simulation of molecular oxygen in an adiabatic cell filled with 1 million DSMC simulator particles and periodic boundaries is performed. Collisions are processed with the variable hard sphere (VHS) model [4] with the properties at a reference temperature T_{ref} of 273 K, i.e. $m = 53.12 \times 10^{-27}$ kg, $d = 4.07 \times 10^{-10}$ m and $\omega = 0.77$. The population of each quantum level is sampled for 1000 time-steps and recorded for three different temperatures: 5,000 K, 10,000 K, and 15,000 K.

The HO and aHO results for the analytical and *dsmcFoam+* calculations are shown in Fig. 4, with the numerical results in excellent agreement with the analytical solutions. Some scatter is evident at the tails of the distributions, particularly for 5,000 K. This is expected in a DSMC simulation, because the probability of finding a molecule in these higher vibrational levels is relatively small, leading to a low signal-to-noise ratio. It is a positive outcome to notice the change from linear to non-linear shape when the aHO model is considered. This crucial characteristic of an aHO model of having higher-lying vibrational quantum levels with a greater population can have an impact on the dissociation of reactive chemical species, however, such phenomena will not be covered in the current work.

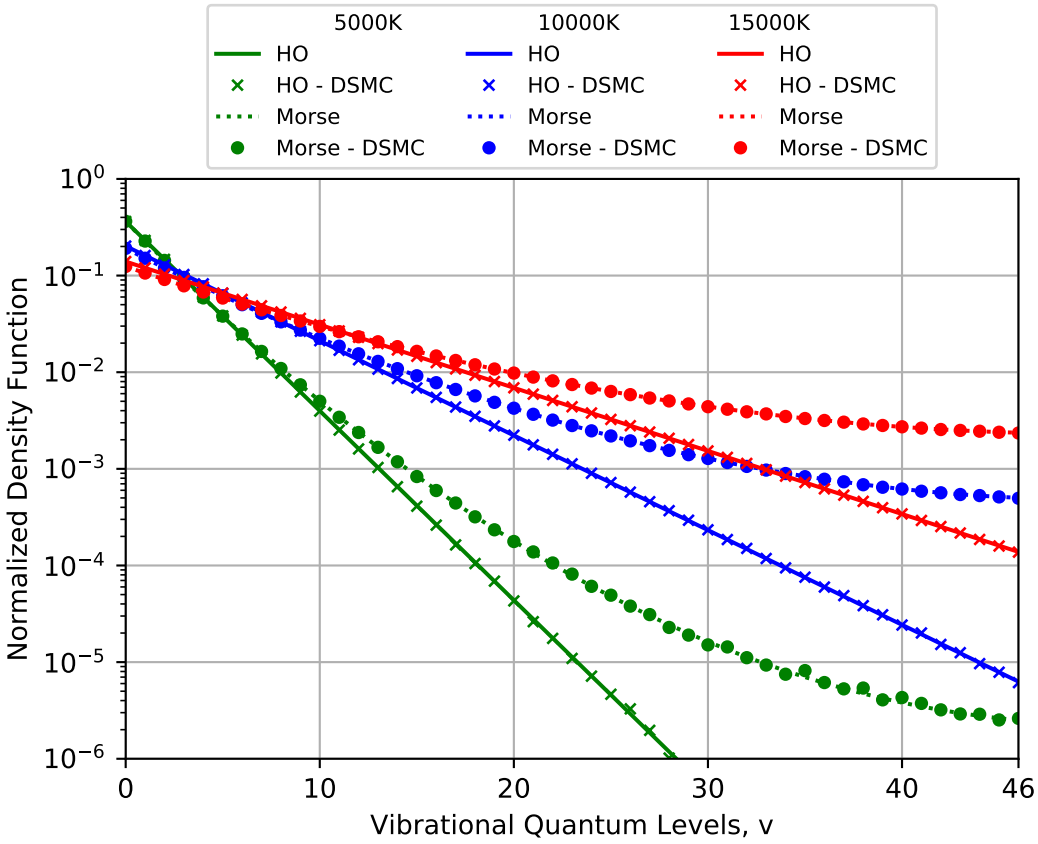

Fig. 4 Probability distribution of vibrational quantum levels for molecular oxygen at the ground state.

IV. Adiabatic Box

A. Partition function

In statistical thermodynamics [3, 60], the parameter that relates internal structures of the molecules to macroscopic properties such as pressure, the temperature, or specific heat capacity, is the partition function, Q, that is defined in terms of the sensible energy, i.e. relative to the zero-point energy,

$$Q(T) \equiv \sum_i g(i) e^{\frac{-\epsilon(i)}{kT}}, \tag{21}$$

where g_i is the degeneracy of the mode and ϵ is the energy of the mode.

In the current work, each mode has been treated individually, i.e. no coupling is considered, therefore it is a matter of evaluating each contribution as a separate element. Translational, rotational, and electronic modes are fully derived in Refs. [2, 3, 60]. In this work the focus is on the vibrational contribution while describing the vibrational excitation of a molecule with a HO or aHO model.

In the HO formalism, the complete derivations of the total mean vibrational energy, $E_v(T_v)$, the degrees of freedom,

$\xi_v(T_v)$, and the specific heat capacity, $C_v^{vib}(T_v)$, are readily obtained with the first and second derivative, with respect to T, of the partition function. The full derivation of these quantities can be found in Refs. [2, 3, 60].

B. Vibrational temperature

The challenge with an aHO model is related to the characteristics of the model presented in Sec. II. By definition, the vibrational partition function follows the formulation in Eq. (21),

$$Q_v^{aHO}(T_v) = \sum_i e^{\frac{-\epsilon_v(i)}{kT_v}}. \tag{22}$$

Because of the nature of vibrational energy in aHO models, the upfront summation can not be dropped and Eq. (22) is lying in its simplest form. Following the whole process with the assessment of the total mean vibrational energy, this quantity is, again, not obtainable with an analytical expression in the same fashion as the HO model, and takes the form,

$$E_v^{aHO}(T_v) = \frac{\sum_i \epsilon_v(i) e^{\frac{-\epsilon_v(i)}{kT_v}}}{\sum_i e^{\frac{-\epsilon_v(i)}{kT_v}}}. \tag{23}$$

Finally, with the degrees of freedom of the molecule being linearly linked to Eq. (23), the expression is,

$$\xi_v^{aHO}(T_v) = \frac{1}{2T_v} \frac{\sum_i \epsilon(i) e^{\frac{-\epsilon(i)}{kT_v}}}{\sum_i e^{\frac{-\epsilon(i)}{kT_v}}}. \tag{24}$$

A point should be made about the calculation of the vibrational temperature, T_v. Through a series of calculations, illustrated in Refs. [1, 2], this quantity is related to the mean vibrational quantum level $< i >$ and the characteristic vibrational temperature of the molecule, θ_v. As a consequence of the simplest form of the vibrational energies, the HO model benefits from a simple derivation and the vibrational temperature can be calculated as

$$T_v^{HO} = \frac{\theta_v}{ln(1 + \frac{1}{<i>})}. \tag{25}$$

An aHO model does not benefit from an analytical expression of T_v and the only way to obtain this parameter is to make use of an iterative methodology to approach one of the quantities derived above. In the current work, a new way of solving this issue is proposed; using a first-order Newton iterative methodology [61, 62] coupled with an optimized pre-loop to hasten the convergence of the approach. A general illustration of the method is represented in Fig. 5. This method is versatile, has fast convergence, and consumes little computational resources [61, 62]. It consists of applying a Taylor expansion around a certain value and truncating the term beyond the fist order. As the series is shortened to conserve only first order terms, the function must be smooth to be approached by a reasonable tangent approximation. In the case of the resolution of T_v for an aHO model, the function $f(T_v)$, in Fig. 5, chosen is composed of the total mean

vibrational energy, Eq. (23), and the value returned by *dsmcFoam+*, E_v^{DSMC},

$$f(T_v) = E_v^{DSMC} - E_v^{aHO}(T_v). \tag{26}$$

The function in Eq. (26) is monotone, which by definition does not contain local minima. Therefore, solving the problem of the vibrational temperature by a Newton iterative method is particularly well adapted since it will not encounter any singularities. Nevertheless, this method is sensitive to the initial value set at the beginning of the process and a coarse initial value can delay convergence.

To avoid this, an optimized pre-Newton loop has been designed to closely approach the value given by *dsmcFoam+* with a scanning process. Once this initial guess is known, the value is passed to the main Newton loop to refine the vibrational temperature value by comparing the gradient of the function, the function itself, and the initial guess to a tolerance factor. In this work, the Newton iterative approach has been applied to a certain function that is related to $E_v(T_v)$. In a different configuration, this versatile method can be employed to solve any irreversible problem as long as the function is smooth. To sum up the implementation requirements of this functionality within a DSMC framework, the user must specify:

- a temperature step, dT – for the pre-loop optimisation, the smaller the better;
- a tolerance factor, α – for the comparison between a gradient, the function, and the initial guess.

C. Vibrational degrees of freedom

In Sec. IV.B, the HO and aHO models have been compared, with a focus on the numerical methodologies employed for the computation of the thermophysical properties. Here, these quantities are studied for a pure oxygen gas experiencing a large range of temperature to investigate the influence of the vibrational models.

Looking first at the vibrational partition function, $Q_v(T_v)$, Eq. (21) is shown in Fig. 6, along with the results extracted from PES calculations [45].

From the beginning of the article, the validity of the HO model at low temperature has been stressed. It is relatively evident in Figs. 6, 7, and 8 that at low-to-moderate temperatures the HO model returns a valid approximation of the vibrational partition function. However, as the temperature increases, the discrepancy between the HO and aHO models becomes appreciable. This departure is, of course, propagated over the quantities derived from the partition function, such as the total mean vibrational energy, in Fig. 7, and the vibrational degrees of freedom, Fig. 8. Although expected, it is good to notice that the value of these quantities returned by *dsmcFoam+* matches the theory, validating the implementation of the aHO model. A second element that should be highlighted is the change of behaviour when switching from HO to aHO in Figs. 7 and 8. In the HO hypothesis, the vibrational degrees of freedom of the diatomic molecule is asymptotically limited to a value of 2, while in the aHO formalism, an oxygen molecule can reach another

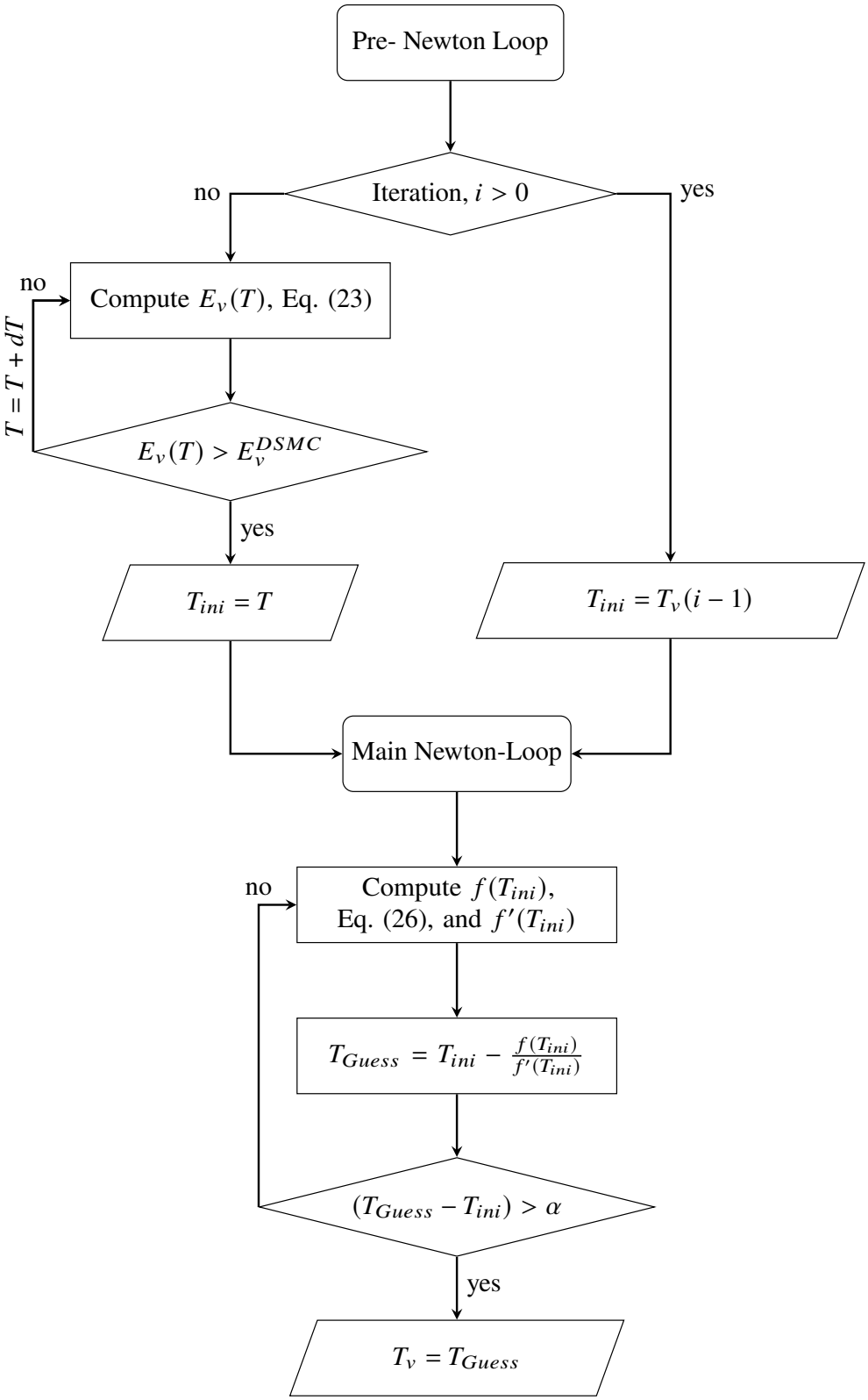

Fig. 5 Flowchart of the first-order Newton approach with an optimized pre-loop.

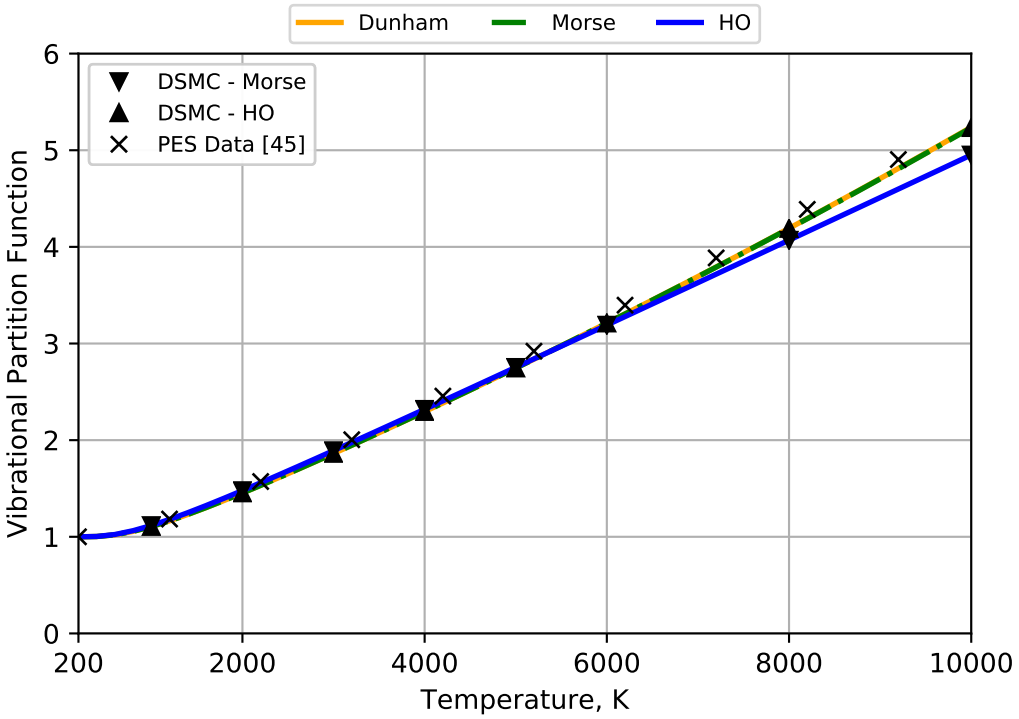

Fig. 6 Partition function, $Q(T_v)$, for HO and aHO models of molecular oxygen.

vibrationally excited state that has more than 2 degrees of freedom over a specific interval of temperature. This behaviour, although still observable within a molecular nitrogen system, is primarily enabled by the weak bond that links the two atoms of oxygen. This modification in the description of the vibrational excitation of the molecule consequently impacts the internal properties of a molecular system.

D. Thermal equilibrium

In this section, a more complex test case is investigated. The HO and aHO models are employed to model the vibrational modes of a diatomic molecule experiencing relaxation from an initial condition of significant thermal non-equilibrium. This situation is simulated with the *dsmcFoam+* solver [38], see Sec. III. The test case is a single adiabatic cell filled with one million DSMC simulator particles with periodic boundaries. The working gas is molecular oxygen. The translational and rotational modes are initialised at 20,000 K, while the vibrational and electronic modes are set at 0 K. The internal energy is redistributed through a serial application of the quantum LB method [52]. The vibrational relaxation rate Z_{ref} is calculated from Eq. (18) with the reference temperature set to $T_{ref} = 20,000$ K. A fraction of $1/5$ and $1/50$ collisions are allowed to result in rotational and electronic relaxation, respectively. In the cell, the collision rate and the corresponding temperature of each internal mode are recorded and presented in Fig. 9. The 'collision number' for the abscissa is calculated as the product of the instantaneous collision rate from the simulation and the physical time that has elapsed [63, 64]. In addition, the CPU time and the memory consumption for both cases

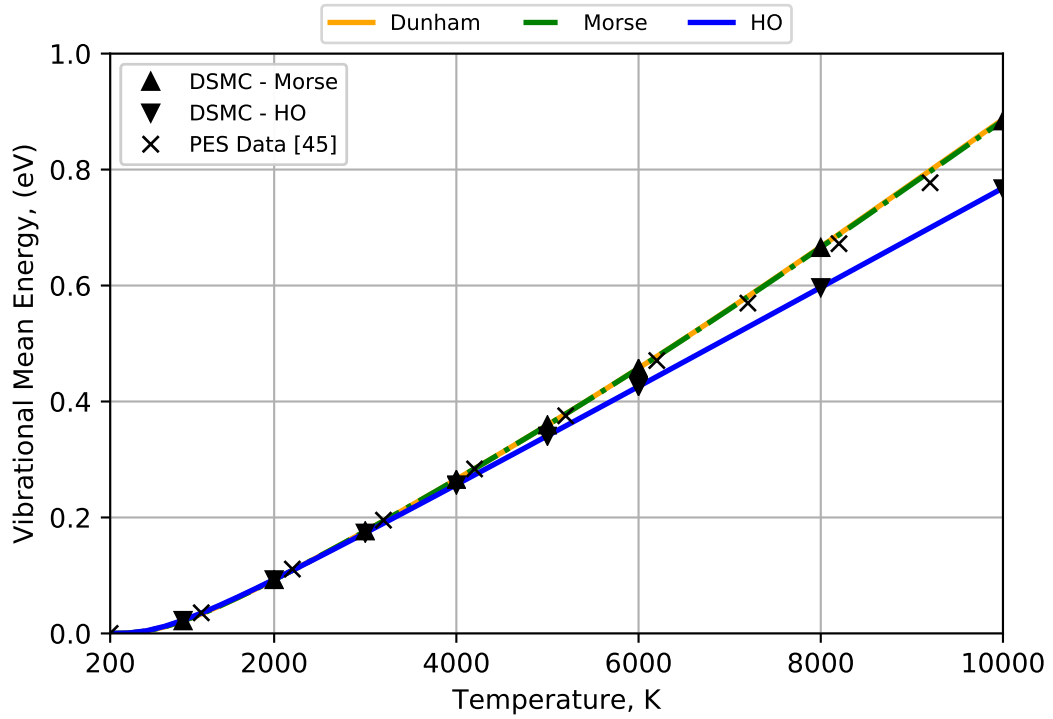

Fig. 7 Total mean vibrational energy, $E_v(T_v)$, for the HO and aHO models of molecular oxygen.

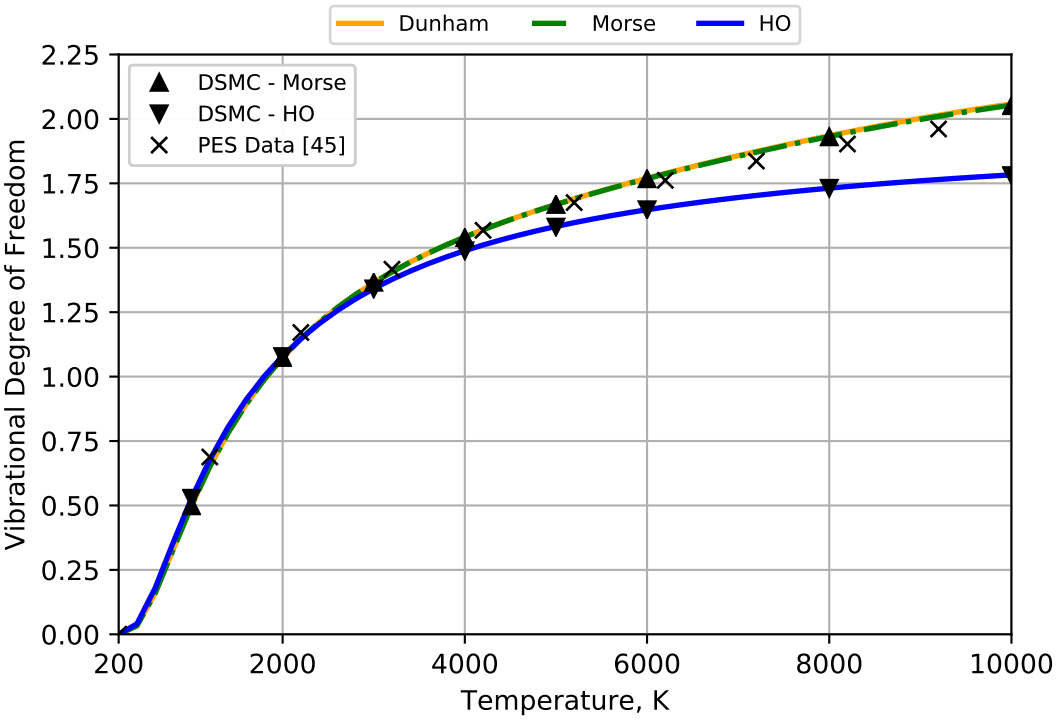

Fig. 8 Vibrational degrees of freedom, $\xi_v(T_v)$, for the HO and aHO models of molecular oxygen.

are monitored and tabulated in Table 6.

Table 6 Numerical expense of aHO and HO models.

Model	CPU time $(s)/100\Delta t$	RAM (GB)
HO	1382.55	0.816
aHO	1385.25	0.816

The major change between the HO model and the aHO model lies in the calculation of the vibrational temperature with a non-linear system to solve in the Morse-aHO framework. Changing from the HO to the aHO model requires some effort in terms of modifying the algorithms, however the methodology used here to implement an aHO model within a DSMC solver is fast and efficient and does not affect the computational expense, as shown in Table 6.

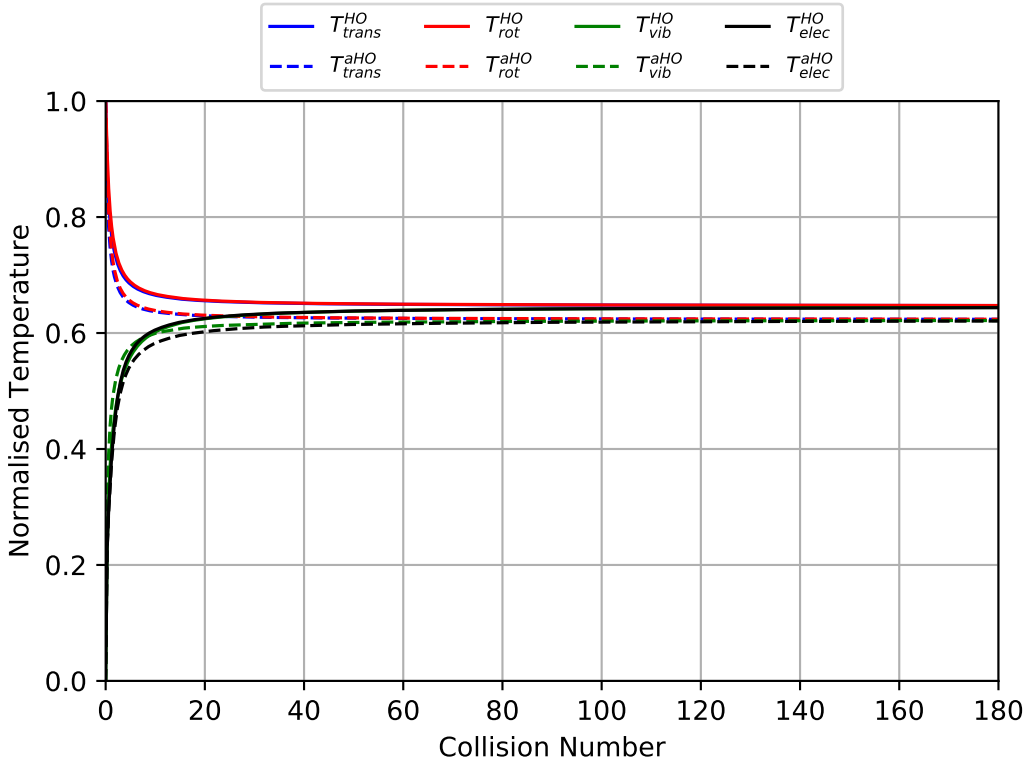

Fig. 9 Simulation of thermal relaxation in pure oxygen gas.

Fig. 9 highlights the difference in terms of the equilibrium state reached at the end of a relaxation process between HO and aHO. The internal mode temperatures are normalised by the initial temperature given to the translational mode. In Fig. 9, the abscissa has been consciously cropped to a collision number of 180 in order to visualise the influence of the Morse-aHO model on the relaxation process at low values of the collision number; the temperatures eventually come in to thermal equilibrium after enough collisions have occurred. A slight increment of 500 K differentiates these two models at equilibrium. The change of the equilibrium temperature is readily derived from the degrees of freedom of the

molecule, Fig. 8, and the corresponding mean energy, Fig. 7. In the case of the aHO model, the molecule is slightly more excited than when an HO model is used ($\xi_v^{aHO}(T_{eq}) > \xi_v^{HO}(T_{eq})$). With the cell being adiabatic, energy is conserved along the relaxation process. The thermal equilibrium must, consequently, reach a lower value for the aHO model.

E. Specific heat capacity

Another thermophysical property that should be regarded while changing from the HO to the aHO model is the specific heat capacity, C_v. The evaluation of the influence of the vibrational model is studied for a pure molecular oxygen gas for a low-to-moderate range of temperature. Often omitted [21, 37, 65–68] in the description of the molecular modes in DSMC simulations, the electronic mode effects on C_v are also highlighted.

By definition, the partition function, $Q(T)$, is related to the specific heat capacity through the second derivative with respect to T,

$$C_v(T) \equiv \frac{\partial^2 Q(T)}{\partial T^2}. \tag{27}$$

The total specific heat capacity of a gas is described as the summation of each of the internal contributions,

$$C_v(T) = C_v^{trans} + C_v^{rot} + C_v^{vib} + C_v^{elec}. \tag{28}$$

In the case of translational and rotational contributions, the corresponding heat capacities, C_v^{trans} and C_v^{rot} are known [2] to be $\frac{3}{2}R$ and R, respectively, where R is the specific gas constant. For the vibrational and electronic modes, this simple form is not readily obtained and requires a full derivation of the partition function, Eq. (22) and Eq. (21), for the vibrational and electronic modes, respectively. By substituting these quantities in Eq. (28), the complete description of the specific heat capacity takes the form,

$$C_v(T) = \frac{3}{2}R + R + \frac{\partial^2 Q^{vib}(T)}{\partial T^2} + \frac{\partial^2 Q^{elec}(T)}{\partial T^2}. \tag{29}$$

Fig. 10 compares the specific heat capacity of molecular oxygen where vibrational excitation is described with the HO and the Morse-aHO models, with the electronic mode being either enabled, including the first six excited states of the oxygen molecule [43, 59], or disabled. Experimental data from the NIST database [43] is included for comparison, along with the Jaffe calculations [69].

Fig. 10 shows the importance of including the electronic mode within the $C_v(T)$ calculation. Even in the situation of an aHO model applied to describe vibrational excitation, the specific heat capacity of the gas does not match experimental data from the NIST-JANAF database [43] or Jaffe calculations [69] for temperatures above 2000 K. Note that adding the electronic contribution to $C_v(T)$ is a significant improvement even under the HO assumption. The best option to recover the experimental data for C_v at low-to-moderate temperatures is the aHO model with the inclusion of

the electronic mode. At high temperature, especially for species with low dissociation energy, the assumption of having four individual modes meets its validity domain. A slight difference between the aHO model and experimental data is noticeable at higher temperatures and is possibly related to the coupling between the rotational and the vibrational modes of the molecules [70]. The vibrational energy list for the excited states also differs from that in the ground state, see Ref. [41], but we have assumed they remain constant in the current work, which will also influence the degree of disagreement here. In the current work, each of the modes have been considered separately and attributed a dedicated partition function. Consequently, this demonstration highlights the necessity of neglecting any modes in the calculation of thermophysical properties, even for relatively low enthalpies, and the requirement of coupling some of the internal modes for a better description of the high enthalpy physics of the flow. It should be reiterated that chemical reactions are not considered in the current work and that the agreement between aHO with electronic excitation and the experimental data is reasonable until well above the expected dissociation temperature of molecular oxygen.

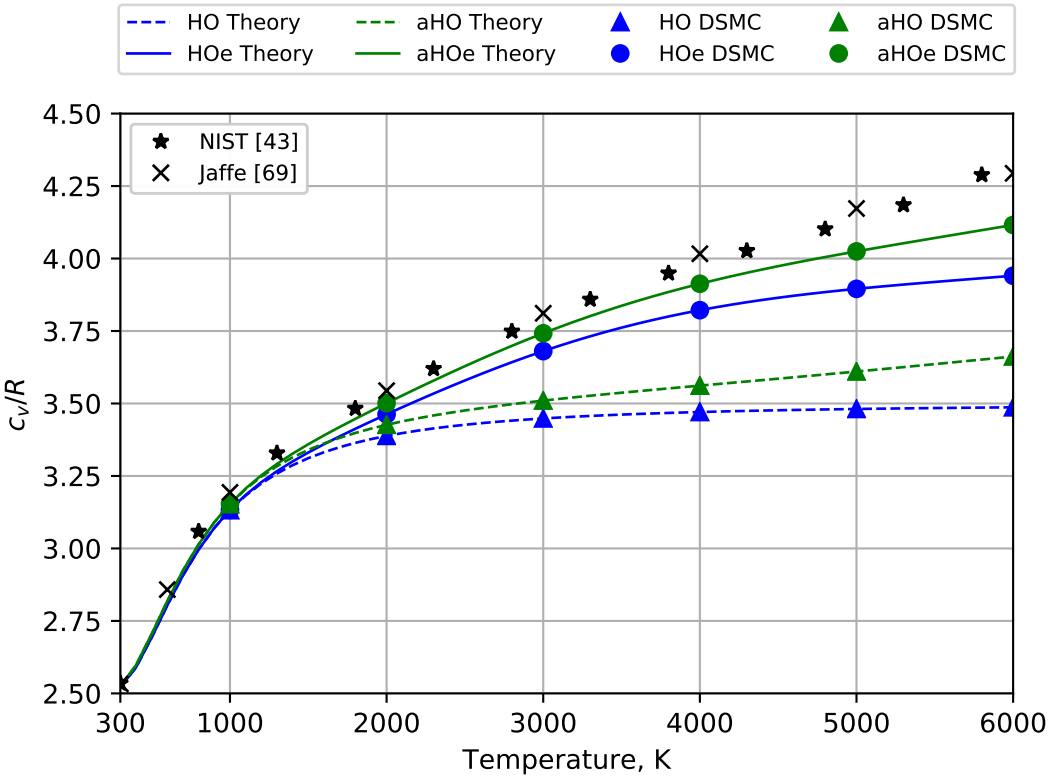

Fig. 10 Specific heat capacity variation with temperature for pure oxygen gas.

V. Hypersonic Cylinder Flow

In order to show the difference between the HO and the aHO models in a 2D hypersonic flow, a study of flow past a cylinder is considered. The free stream conditions are $Ma_\infty = 16$, $P_\infty = 48.5$ Pa, $T_\infty = 300$ K. The cylindrical body has

a diameter of $D = 0.01$ m, giving $Kn_D = 0.005$. The working gas is non-reacting molecular oxygen. The electronic energy follows the techniques developed by Liechty [59]. The redistribution of internal energies is modelled by a serial application of the quantum Larsen-Borgnakke method [52] using the HO model or the Morse-aHO model. The inter-molecular collisions are computed by the variable hard sphere (VHS) model [4] with a reference temperature of $T_{ref} = 273$ K. A constant fraction of $1/5$ and $1/50$ collisions are considered for rotational and vibrational relaxation, respectively. Additionally, two fractions of collisions, $1/100$ and $1/500$, are considered for the relaxation of the electronic mode.

The geometry represents a 2D slice of a cylinder with a domain length equal to one diameter upstream of the stagnation point. The mesh is refined near the stagnation point to ensure a cell size, Δx, of around one quarter of the local mean free path, λ, is maintained, resulting in a total of $152,123$ cells. The gas-surface interactions are fully diffusive with a wall temperature, $T_w = 300$ K. The time-step, Δt, is carefully chosen following Eq. (30),

$$\Delta t = \begin{cases} \frac{1}{10} \times \frac{\Delta x}{u_\infty} & \text{if } \frac{\Delta x}{u_\infty} \leq \frac{\lambda_2}{c_w} \\ \frac{1}{10} \times \frac{\lambda_2}{c_w} & \text{if } \frac{\Delta x}{u_\infty} \geq \frac{\lambda_2}{c_w} \end{cases} \tag{30}$$

where u_∞ is the free stream velocity, λ_2 is the VHS mean free path [71] downstream of the normal shock wave that develops along the stagnation streamline, c_w is the most probable thermal velocity [2] such that,

$$c_w = \sqrt{2RT_2}, \tag{31}$$

where T_2 is the peak value of the translational temperature along the stagnation streamline. Based on this, a time step of 10^{-9}s was used, which is smaller than the smallest values of both the mean collision time and the cell residence time.

The simulation was run in parallel on 6 AMD® Ryzen 9 5950x CPU cores (base: 3.4GHz, max: 4.9 GHz) and over $300,000$ samples are taken after steady-state to reduce the numerical scatter. The temperatures along the stagnation streamline are presented in Fig. 11. The translational, rotational, and vibrational temperature contours are shown in Figs. 14, 12, and 13, respectively. The inclusion of the electronic mode is denoted by HOe and $aHOe$.

A. Stagnation Line Properties

The influence of the vibrational models on the internal temperatures along the stagnation streamline is plotted in Fig. 11. The internal temperatures are normalised by the free stream temperature and the longitudinal coordinate is normalised by the diameter of the cylinder. The peak values and their locations are summarised in Table 7.

Physically, the flow experiences a compression through the shock wave that forms in front of the body. The internal modes are consequently largely activated throughout the shock, culminating in a peak value downstream of the shock wave. The dominating mode is naturally the translational energy, Fig. 11a, which experiences a steep increase across

Table 7 Comparison of the HO model and aHO model on the peak value of the internal temperatures and their locations. The inclusion of electronic energy is denoted by HOe and aHOe.

Model	$\frac{x}{D}\|_{max(T_t)}$	$\frac{T_t}{T_\infty}$	$\frac{x}{D}\|_{max(T_r)}$	$\frac{T_r}{T_\infty}$	$\frac{x}{D}\|_{max(T_v)}$	$\frac{T_v}{T_\infty}$	$\frac{x}{D}\|_{max(T_e)}$	$\frac{T_e}{T_\infty}$
HO	-0.31	56.48	-0.23	44.64	-0.10	38.43	-	-
aHO	-0.30	56.31	-0.23	44.08	-0.10	37.05	-	-
$HOe^{Z_e=500}$	-0.30	56.35	-0.23	44.32	-0.10	37.29	-0.06	19.51
$aHOe^{Z_e=500}$	-0.29	56.33	-0.23	43.81	-0.10	36.24	-0.06	19.51
$HOe^{Z_e=100}$	-0.29	55.98	-0.23	43.28	-0.10	35.85	-0.08	31.78
$aHOe^{Z_e=100}$	-0.28	55.87	-0.22	42.35	-0.10	35.01	-0.08	31.21

the shock wave and reaches a peak value upstream the body surface. It undergoes a short relaxation process before enduring a rapid drop towards the constant value of the cylinder surface temperature. The small difference of the thermal peak value between the two vibrational energy models originates from the nonlinear distribution of vibrational energy over the vibrational quantum levels as seen in Sec. III. The inclusion of electronic mode results in a small drop of the translational temperature in similar proportion to the modelling of the vibrational excitation with an aHO model.

The rotational mode is the most dominant internal mode of the molecule and the profiles through the stagnation streamline are shown in Fig. 11b. The rotational temperature exhibits a smaller peak of temperature in comparison with the translational temperature. It initiates a relaxation process before undergoing a sudden decrease towards the body surface. The inclusion of the electronic energy results in a peak value of rotational temperature that is 100 K lower for $Z_e = 500$ and 400 K lower for $Z_e = 100$ than the predicted state with the electronic mode disabled. This finding is directly linked to the addition of a fourth channel for the energy, resulting in a lower thermal state, as was noted in Sec. IV.D.

The vibrational temperature peaks closer to the surface compared to the translational and rotational modes, as is shown in Fig. 11c. The vibrational temperature exhibits a parabolic shape and does not have the time to relax towards a quasi-transient thermal equilibrium state with the translational temperature until near the surface of the cylinder. The aHO model results in a smaller vibrational temperature peak compared to the HO model. This behaviour is partly due to the non-linear distribution of the vibrational energy over the vibrational quantum levels. At high temperatures, the Morse-aHO model suggests that the high lying vibrational quantum levels become significantly more populated than in the HO model. This overpopulation at the end of the vibrational quantum ladder decreases the vibrational temperature. Similarly, the inclusion of electronic energy considerably impacts the vibrational temperature across the shock wave, with the result of a lower peak value compared to the HO profile. Note that the larger electronic relaxation probability results in a smaller vibrational temperature peak value. Fig. 11c also shows that the new measurement technique for the vibrational temperature when using the aHO model works well in flows with large spatial gradients of temperature.

In this study the electronic temperature is calculated with the approach developed by Liechty [59] and derived from the ratio of the Boltzmann distribution of the ground state and the first unbounded electronic states. The assumption of

the higher lying electronic states having a negligible contribution is applied here. Although this model is a zeroth-order approximation of the electronic temperature and the electronic degrees of freedom, it has significantly improved the calculation of the thermophysical flow properties, i.e. specific heat capacity, see Fig. 10. When the electronic mode relaxes with $Z_e = 100$, the electronic temperature has a larger peak value and the inclusion of the electronic mode significantly impacts the vibrational temperature profile. For the other relaxation constant value, i.e. $Z_e = 500$, the electronic temperature reaches smaller a peak value, inducing a lower impact on the other internal modes of the molecule.

B. Thermal Non-Equilibrium

In the previous section, the comparison of the two vibrational models was limited to the stagnation line properties and the results show that the Morse-aHO model results in lower thermal peak values. In Figs. 12, 13, and 14, the translational, rotational, and vibrational temperature contours, respectively, are plotted for the two vibrational models and the electronic mode enabled with the two relaxation constants denoted $()^{Z_e=100}$ and $()^{Z_e=500}$.

From Fig. 12 it is evident that the vibrational models agree well in the far-field region and the near the surface of the body. However, in the vicinity of the shock wave, the Morse-aHO model predicts a slightly smaller shock stand off distance. When the electronic mode is enabled, the peak temperature decreases and the shock stand off distance agrees between HO and aHO.

Fig. 13 shows that the rotational temperature exhibits notable changes in its topology when the Morse-aHO model is applied and the electronic mode is activated. Similar to the translational temperature, the two models result in differences in the region where the shock wave develops. In this region, the HO model results in larger and more diffuse high-temperature contours compared to the Morse-aHO model. The addition of the electronic mode tends to reduce the discrepancy between the two models; although, the Morse-aHO model predicts a significantly smaller very-high temperature contour with the highest electronic relaxation constant.

When the electronic mode is disabled, Figs. 14a and Fig. 14d show a reasonable agreement for the first six contours where the vibrational temperature does not exceed $6,000$ K. For any temperature above this value, the aHO model shows smaller areas bounded by the contours. This behaviour is gradually accentuated as the temperature increases. In addition to a difference in the high temperature areas, the two models also differ in the peak temperature that is achieved. The HO model results in a higher temperature ratio of 38.43 whereas the aHO model peaks at 37.05, as seen in Table. 7. Note that this result agrees with the observations from Figs. 6, 7, and 8, in which the aHO model returned a larger value of the vibrational degrees of freedom than the HO model, i.e. $\xi_v^{aHO}(T_{eq}) > \xi_v^{HO}(T_{eq})$. As a result, the mean vibrational energy calculated by the aHO model is lower, which leads to a lower vibrational temperature and smaller high-temperature areas.

The inclusion of the electronic mode changes the topology of the vibrational temperature. For $Z_e = 500$, the high-temperature contour layers reduce in size compared to when the electronic mode is omitted. For $Z_e = 100$, the

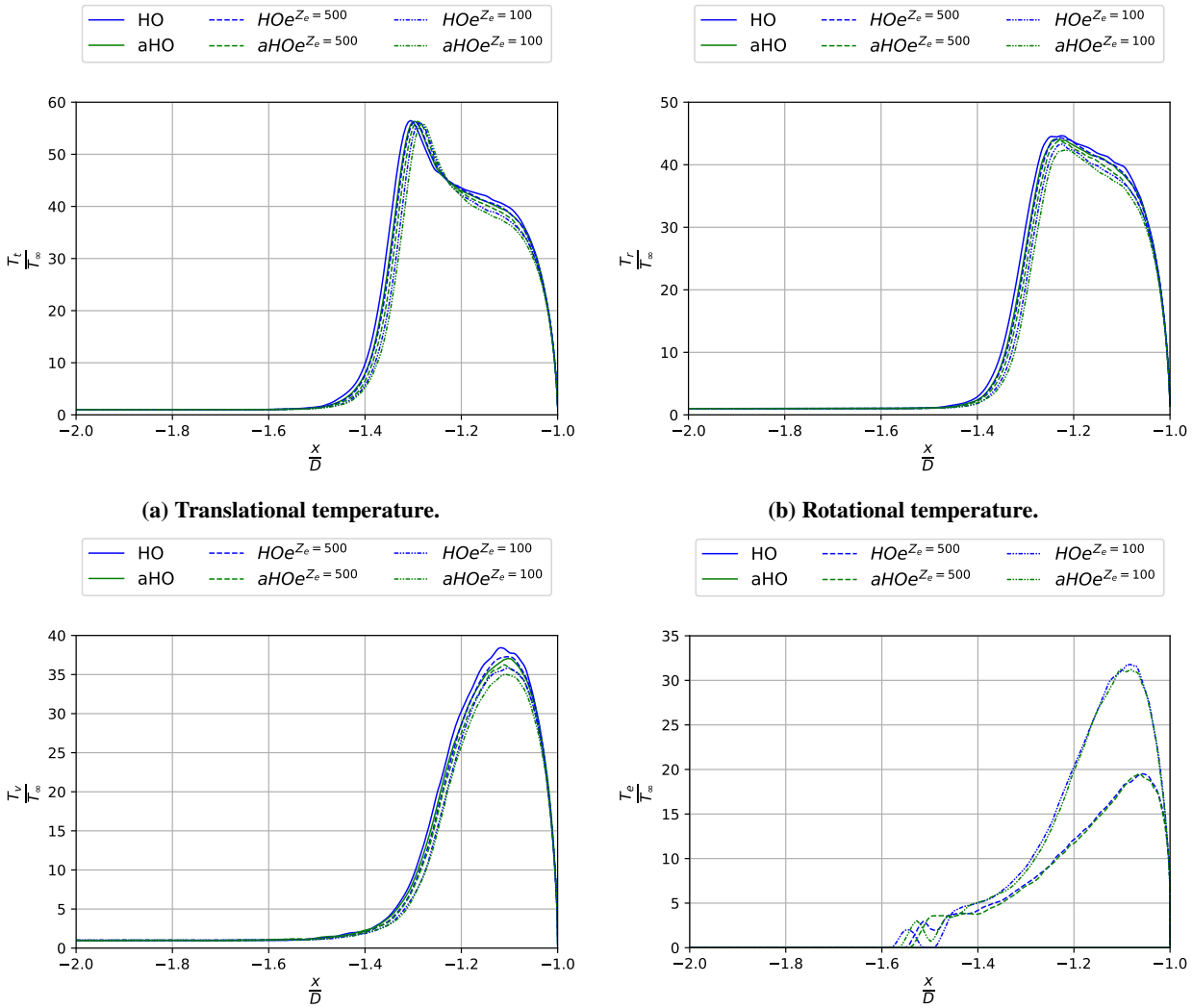

(a) Translational temperature.

(b) Rotational temperature.

(c) Vibrational temperature.

(d) Electronic temperature.

Fig. 11 Temperatures along the stagnation streamline for pure oxygen gas flow over a cylinder with free stream conditions $Ma_\infty = 16$ and $Kn_D = 0.005$. The inclusion of electronic energy is denoted by HOe and aHOe in the legend.

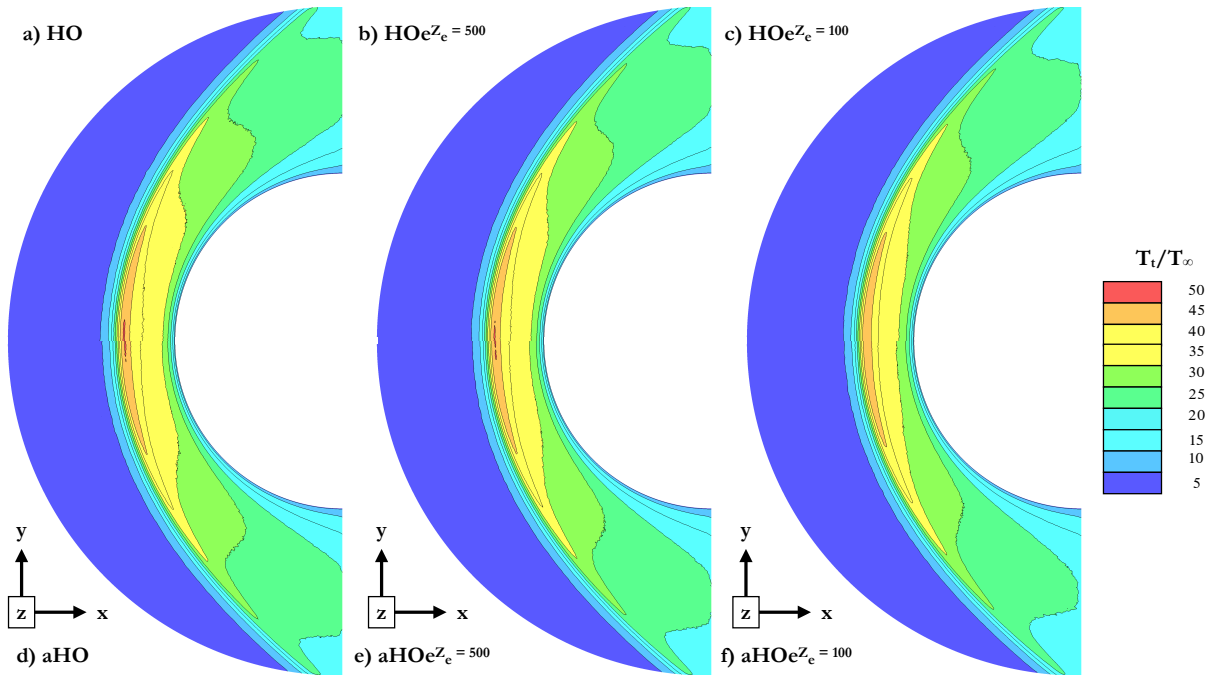

Fig. 12 Non-dimensionalised translational temperature contours for hypersonic flow over a cylinder; a) harmonic oscillator and no electronic energy, b) harmonic oscillator with electronic energy and $Z_e = 500$, c) harmonic oscillator with electronic energy and $Z_e = 100$, d) anharmonic oscillator and no electronic energy, e) anharmonic oscillator with electronic energy and $Z_e = 500$, f) anharmonic oscillator with electronic energy and $Z_e = 100$.

high-temperature regions are strongly impacted resulting in considerably smaller contours. This implies a significant decrease in the vibrational temperature around the cylindrical body when the electronic mode is enabled. The inclusion of the electronic mode constitutes another sink in which to redistribute the internal energy, which, in turn, decreases the internal energy allocated to the vibrational mode. As has been highlighted in Fig. 10, the inclusion of unbounded electronic states has a significant impact on the thermophysical flow properties and results in a better description of the physics of the flow. When the unbounded electronic mode is activated, Figs. 14b, 14c, 14e and Fig. 14f, the peak value of the vibrational temperature changes and the contours significantly reduce in area. The two vibrational models agree very well in the vicinity of the stagnation point and the far-field regions providing similar areas for all the contours. which is expected as the temperature in these regions is much lower.

VI. Conclusions

The merits of different vibrational models for use in DSMC simulations have been discussed and analysed. The harmonic oscillator model is simple to implement and has been shown to be a good approximation for low enthalpy flows. At higher enthalpies, it is clear that an anharmonic oscillator model offers a better description of the flow physics. The Morse-aHO model has been implemented within *dsmcFoam+* and validated with the reproduction of fundamental parameters, such as the mean vibrational energy, degrees of freedom, and thermophysical properties of a

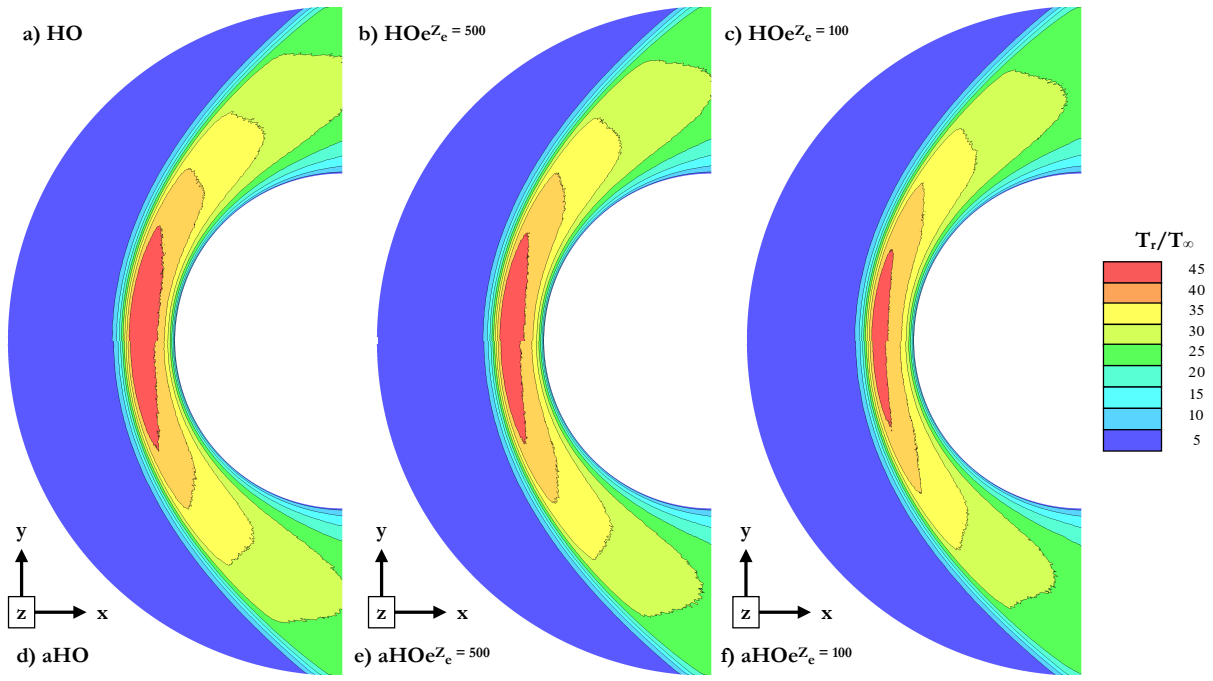

Fig. 13 Non-dimensionalised rotational temperature contours for hypersonic flow over a cylinder; a) harmonic oscillator and no electronic energy, b) harmonic oscillator with electronic energy and $Z_e = 500$, c) harmonic oscillator with electronic energy and $Z_e = 100$, d) anharmonic oscillator and no electronic energy, e) anharmonic oscillator with electronic energy and $Z_e = 500$, f) anharmonic oscillator with electronic energy and $Z_e = 100$.

gas. Additionally, a method for returning a macroscopic measurement of the vibrational temperature of a gas when using the aHO model is described.

Relaxation to thermal equilibrium has been demonstrated using a serial Larsen-Borgnakke model to redistribute energy between the various modes and it is shown that the aHO model results in a slightly lower equilibrium temperature. The importance of including the electronic mode for reproducing the correct thermophysical properties has been illustrated and it is shown that the aHO model improves this prediction further over an HO model. The study of a hypersonic flow past a cylindrical body has shown that the vibrational temperature is over-estimated when considering the HO model. Similarly to the specific heat capacity study, the vibrational temperature is substantially impacted by the omission of the electronic mode. The Morse-aHO model needs further improvement to bring the model into closer alignment with experimental data. However, it seems that modelling the vibrational excitation with an aHO model and including the unbounded electronic states offers a more accurate description than only representing the molecular vibrations using the HO model.

In future work, further studies on the coupling between the rotational and the vibrational modes will be presented. The influence of having different lists of vibrational energy for each excited state of a molecule will also be explored. Additionally, investigations on the influence of modelling the vibrational excitation with an aHO model on chemical

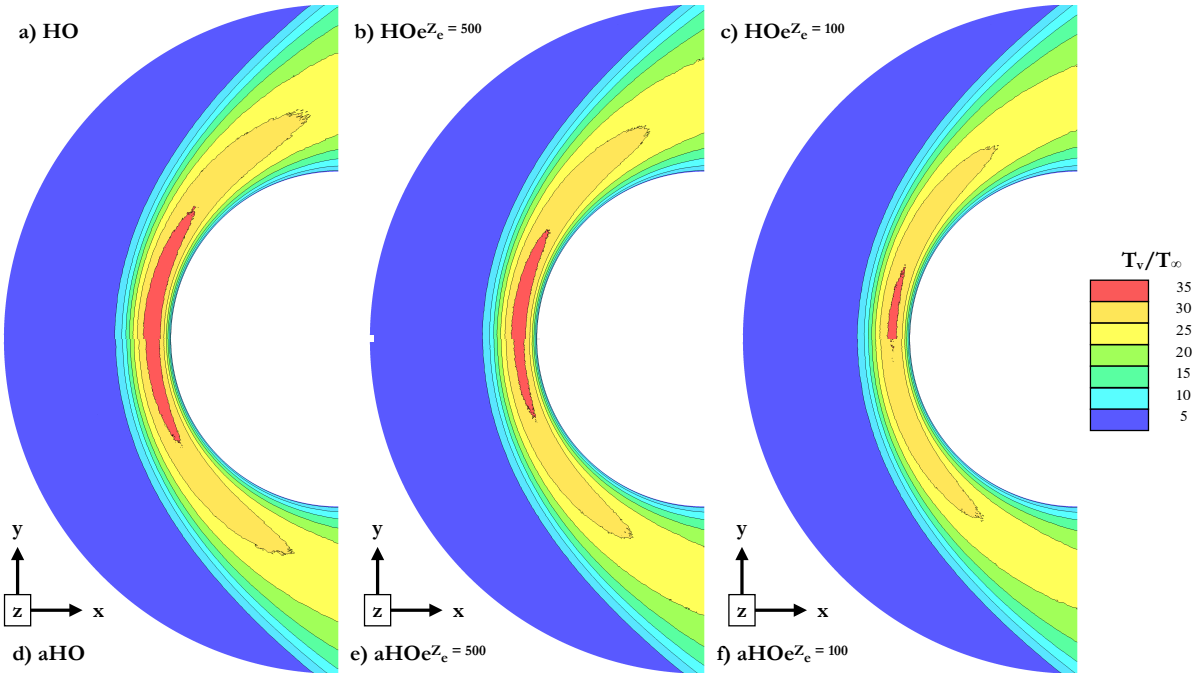

Fig. 14 Non-dimensionalised vibrational temperature contours for hypersonic flow over a cylinder; a) harmonic oscillator and no electronic energy, b) harmonic oscillator with electronic energy and $Z_e = 500$, c) harmonic oscillator with electronic energy and $Z_e = 100$, d) anharmonic oscillator and no electronic energy, e) anharmonic oscillator with electronic energy and $Z_e = 500$, f) anharmonic oscillator with electronic energy and $Z_e = 100$.

reaction rates will be addressed.

Funding Sources

The author gratefully acknowledges scholarship funding from the James Watt School of Engineering.

References

[1] Anderson, J. D., *Hypersonic and high-temperature gas dynamics*, American Institute of Aeronautics and Astronautics, 2006.

[2] Kruger, C. H., and Vincenti, W. G., *Introduction to Physical Gas Dynamics*, John Willey & Sons, 1965.

[3] Liepmann, H. W., and Roshko, A., *Elements of Gas Dynamics*, John Wiley & Sons, 1957.

[4] Bird, G. A., *Molecular gas dynamics and the direct simulation of gas flows*, Oxford Engineering Science Series, 1994.

[5] Boyd, I. D., and Schwartzentruber, T. E., *Nonequilibrium gas dynamics and molecular simulation*, Vol. 42, Cambridge University Press, 2017.

[6] Fasoulas, S., Munz, C.-D., Pfeiffer, M., Beyer, J., Binder, T., Copplestone, S., Mirza, A., Nizenkov, P., Ortwein, P., and Reschke, W., "Combining particle-in-cell and direct simulation Monte Carlo for the simulation of reactive plasma flows," *Physics of Fluids*, Vol. 31, No. 7, 2019, p. 072006. https://doi.org/10.1063/1.5097638.

[7] Kustova, E., Alekseev, I., and Tan, L., "Investigation of shock wave structure in CO_2 based on the continuum and DSMC approaches," *Journal of Physics: Conference Series*, Vol. 1959, IOP Publishing, 2021, p. 012032. https://doi.org/10.1088/1742-6596/1959/1/012032.

[8] Li, Z., Parsons, N., and Levin, D. A., "A study of internal energy relaxation in shocks using molecular dynamics based models," *The Journal of Chemical Physics*, Vol. 143, No. 14, 2015, p. 144501. https://doi.org/10.1063/1.4931107.

[9] Capitelli, M., Colonna, G., Marraffa, L., Giordano, D., Giordano, D., and Warmbein, B., *Tables of internal partition functions and thermodynamic properties of high-temperature Mars-atmosphere species from 50K to 50000K*, European Space Agency, 2005.

[10] Babou, Y., Rivière, P., Perrin, M.-Y., and Soufiani, A., "High-temperature and nonequilibrium partition function and thermodynamic data of diatomic molecules," *International Journal of Thermophysics*, Vol. 30, No. 2, 2009, pp. 416–438. https://doi.org/10.1007/s10765-007-0288-6.

[11] Qin, Z., Zhao, J., and Liu, L., "High-temperature partition functions, specific heats and spectral radiative properties of diatomic molecules with an improved calculation of energy levels," *Journal of Quantitative Spectroscopy and Radiative Transfer*, Vol. 210, 2018, pp. 1–18. https://doi.org/10.1016/j.jqsrt.2018.02.004.

[12] Morse, P. M., "Diatomic molecules according to the wave mechanics. II. Vibrational levels," *Physical review*, Vol. 34, No. 1, 1929, p. 57. https://doi.org/10.1103/PhysRev.34.57.

[13] Dunham, J. L., "The energy levels of a rotating vibrator," *Physical Review*, Vol. 41, No. 6, 1932, p. 721. https://doi.org/10.1103/PhysRev.41.721.

[14] Atkins, P. W., and Friedman, R. S., *Molecular quantum mechanics*, Oxford university press, 2011. https://doi.org/10.1021/ed076p170.2.

[15] Blinder, S. M., *Introduction to quantum mechanics*, Academic Press, 2020.

[16] Kauzmann, W., *Quantum chemistry: an introduction*, Elsevier, 2013.

[17] Roy, R. J. L., "LEVEL: A computer program for solving the radial Schrödinger equation for bound and quasibound levels," *Journal of Quantitative Spectroscopy and Radiative Transfer*, Vol. 186, 2017, pp. 167–178. https://doi.org/10.1016/j.jqsrt.2016.05.028.

[18] Capitelli, M., Colonna, G., Giordano, D., Marraffa, L., Casavola, A., Minelli, P., Pagano, D., Pietanza, L., and Taccogna, F., "High-temperature thermodynamic properties of Mars-atmosphere components," *Journal of Spacecraft and Rockets*, Vol. 42, No. 6, 2005, pp. 980–989. https://doi.org/10.2514/1.12503.

[19] Capitelli, M., Colonna, G., Gorse, C., and Giordano, D., "Thermodynamic Properties of High-Temperature Air Components," *Molecular Physics and Hypersonic Flows*, Springer, 1996, pp. 293–301. https://doi.org/10.1007/978-94-009-0267-1_17.

[20] Colonna, G., Pietanza, L. D., and Capitelli, M., "Recombination-assisted nitrogen dissociation rates under nonequilibrium conditions," *Journal of Thermophysics and Heat Transfer*, Vol. 22, No. 3, 2008, pp. 399–406. https://doi.org/10.2514/1.33505.

[21] Haas, B. L., and Boyd, I. D., "Models for direct Monte Carlo simulation of coupled vibration–dissociation," *Physics of Fluids A: Fluid Dynamics*, Vol. 5, No. 2, 1993, pp. 478–489. https://doi.org/10.1063/1.858870.

[22] Bruno, D., Capitelli, M., and Longo, S., "DSMC modelling of vibrational and chemical kinetics for a reacting gas mixture," *Chemical Physics letters*, Vol. 289, No. 1-2, 1998, pp. 141–149. https://doi.org/10.1016/S0009-2614(98)00399-6.

[23] Koura, K., "Monte Carlo direct simulation of rotational relaxation of nitrogen through high total temperature shock waves using classical trajectory calculations," *Physics of Fluids*, Vol. 10, No. 10, 1998, pp. 2689–2691. https://doi.org/10.1063/1.869782.

[24] Koura, K., "Direct simulation Monte Carlo study of rotational nonequilibrium in shock wave and spherical expansion of nitrogen using classical trajectory calculations," *Physics of Fluids*, Vol. 14, No. 5, 2002, pp. 1689–1695. https://doi.org/10.1063/1.1467059.

[25] Carlson, A. B., and Bird, G. A., "Implementation of a vibrationally linked chemical reaction model for DSMC," Tech. rep., 1994. https://doi.org/10.5555/885978.

[26] Ruffin, S. M., "Prediction of Vibrational Relaxation in Hypersonic Expanding Flows Part I: Model Development," *Journal of Thermophysics and Heat Transfer*, Vol. 9, No. 3, 1995, pp. 432–437. https://doi.org/10.2514/3.685.

[27] Ruffin, S. M., "Prediction of vibrational relaxation in hypersonic expanding flows part 2: Results," *Journal of Thermophysics and Heat Transfer*, Vol. 9, No. 3, 1995, pp. 438–445. https://doi.org/10.2514/3.56309.

[28] da Silva, M. L., Guerra, V., Loureiro, J., and Sá, P. A., "Vibrational distributions in N_2 with an improved calculation of energy levels using the RKR method," *Chemical Physics*, Vol. 348, No. 1-3, 2008, pp. 187–194. https://doi.org/10.1016/j.chemphys.2008.02.048.

[29] Koura, K., "4 Monte Carlo direct simulation of rotational relaxation of diatomic molecules using classical trajectory calculations: Nitrogen shock wave," *Physics of Fluids*, Vol. 9, No. 11, 1997, pp. 3543–3549. https://doi.org/10.1063/1.869462.

[30] Koura, K., "A set of model cross sections for the Monte Carlo simulation of rarefied real gases: Atom–diatom collisions," *Physics of Fluids*, Vol. 6, No. 10, 1994, pp. 3473–3486. https://doi.org/10.1063/1.868404.

[31] Hammerling, P., Teare, J. D., and Kivel, B., "Theory of radiation from luminous shock waves in nitrogen," *The Physics of Fluids*, Vol. 2, No. 4, 1959, pp. 422–426. https://doi.org/10.1063/1.1724413.

[32] Treanor, C. E., and Marrone, P. V., "Effect of dissociation on the rate of vibrational relaxation," *The Physics of Fluids*, Vol. 5, No. 9, 1962, pp. 1022–1026. https://doi.org/10.1063/1.1724467.

[33] Marrone, P. V., and Treanor, C. E., "Chemical relaxation with preferential dissociation from excited vibrational levels," *The Physics of Fluids*, Vol. 6, No. 9, 1963, pp. 1215–1221. https://doi.org/10.1063/1.1706888.

[34] Bender, J. D., Valentini, P., Nompelis, I., Paukku, Y., Varga, Z., Truhlar, D. G., Schwartzentruber, T. E., and Candler, G. V., "An improved potential energy surface and multi-temperature quasiclassical trajectory calculations of N_2^+ N_2 dissociation reactions," *The Journal of Chemical Physics*, Vol. 143, No. 5, 2015, p. 054304. https://doi.org/10.1063/1.4927571.

[35] Liu, Y., Panesi, M., Sahai, A., and Vinokur, M., "General multi-group macroscopic modeling for thermo-chemical non-equilibrium gas mixtures," *The Journal of Chemical Physics*, Vol. 142, No. 13, 2015, p. 134109. https://doi.org/10.1063/1.4915926.

[36] Singh, N., and Schwartzentruber, T., "Non-Boltzmann vibrational energy distributions and coupling to dissociation rate," *The Journal of Chemical Physics*, Vol. 152, No. 22, 2020, p. 224301. https://doi.org/10.1063/1.5142732.

[37] Schouler, M., Prévereaud, Y., and Mieussens, L., "IXV post-flight reconstruction and analysis of the aerothermodynamic measurements along the rarefied portion of the reentry trajectory," *International Journal of Heat and Mass Transfer*, Vol. 178, 2021, p. 121582. https://doi.org/10.1016/j.ijheatmasstransfer.2021.121582.

[38] White, C., Borg, M. K., Scanlon, T. J., Longshaw, S., John, B., Emerson, D. R., and Reese, J. M., "dsmcFoam+: An OpenFOAM based direct simulation Monte Carlo solver," *Computer Physics Communications*, Vol. 224, 2018, pp. 22–43. https://doi.org/10.1016/j.cpc.2017.09.030.

[39] Griffiths, D. J., and Schroeter, D. F., *Introduction to quantum mechanics*, Cambridge university press, 2018.

[40] Huber, K.-P., *Molecular spectra and molecular structure: IV. Constants of diatomic molecules*, Springer Science & Business Media, 2013. https://doi.org/10.1007/978-1-4757-0961-2_2.

[41] Huber, K.-P., "Constants of diatomic molecules," *Molecular spectra and molecular structure*, 1979. https://doi.org/10.1007/978-1-4757-0961-2.

[42] Hulburt, H. M., and Hirschfelder, J. O., "Potential energy functions for diatomic molecules," *The Journal of Chemical Physics*, Vol. 9, No. 1, 1941, pp. 61–69. https://doi.org/10.1063/1.1750827.

[43] NIST, "National Institute for Standards and Technology (NIST) Chemistry WebBook," , 2015. URL https://kinetics.nist.gov/kinetics/index.jsp.

[44] Macheret, S. O., and Adamovich, I. V., "Semiclassical modeling of state-specific dissociation rates in diatomic gases," *The Journal of Chemical Physics*, Vol. 113, No. 17, 2000, pp. 7351–7361. https://doi.org/10.1063/1.1313386.

[45] Armenise, I., and Esposito, F., "N_2, O_2, NO state-to-state vibrational kinetics in hypersonic boundary layers: The problem of rescaling rate coefficients to uniform vibrational ladders," *Chemical Physics*, Vol. 446, 2015, pp. 30–46. https://doi.org/10.1016/j.chemphys.2014.11.004.

[46] Bose, T. K., "High temperature gas dynamics," *High Temperature Gas Dynamics*, Springer, 2004, pp. 259–281.

[47] Schwartzentruber, T. E., and Boyd, I. D., "Progress and future prospects for particle-based simulation of hypersonic flow," *Progress in Aerospace Sciences*, Vol. 72, 2015, pp. 66–79. https://doi.org/10.1016/j.paerosci.2014.09.003.

[48] Dietrich, S., and Boyd, I. D. ., "Scalar and parallel optimized implementation of the direct simulation Monte Carlo method," *Journal of Computational Physics*, Vol. 126, No. 2, 1996, pp. 328–342. https://doi.org/10.1006/jcph.1996.0141.

[49] LeBeau, G. J., "A parallel implementation of the direct simulation Monte Carlo method," *Computer methods in applied mechanics and engineering*, Vol. 174, No. 3-4, 1999, pp. 319–337. https://doi.org/10.1016/S0045-7825(98)00302-8.

[50] Plimpton, S. J., and Gallis, M. A., "SPARTA direct simulation Monte Carlo (DSMC) simulator," *Sandia National Laboratories, USA*, 2015. URL http://sparta.sandia.gov.

[51] Weller, H. C., Tabor, G., Jasak, H., and Fureby, C., "A tensorial approach to computational continuum mechanics using object-oriented techniques," *Computers in Physics*, Vol. 12, No. 6, 1998, pp. 620–631. https://doi.org/10.1063/1.168744.

[52] Borgnakke, C., and Larsen, P. S., "Statistical collision model for Monte Carlo simulation of polyatomic gas mixture," *Journal of computational Physics*, Vol. 18, No. 4, 1975, pp. 405–420. https://doi.org/10.1016/0021-9991(75)90094-7.

[53] Adamovich, I. V., Macheret, S. O., Rich, J. W., and Treanor, C. E., "Vibrational relaxation and dissociation behind shock waves. Part 1-Kinetic rate models." *AIAA Journal*, Vol. 33, No. 6, 1995, pp. 1064–1069. https://doi.org/10.2514/3.48339.

[54] Kulakhmetov, M., Gallis, M., and Alexeenko, A., "Effect of O 2+ O *ab initio* and Morse additive pairwise potentials on dissociation and relaxation rates for nonequilibrium flow calculations," *Physics of Fluids*, Vol. 27, No. 8, 2015, p. 087104. https://doi.org/10.1063/1.4928198.

[55] Kulakhmetov, M., Gallis, M., and Alexeenko, A., "Ab initio-informed maximum entropy modeling of rovibrational relaxation and state-specific dissociation with application to the O_2+O system," *The Journal of Chemical Physics*, Vol. 144, No. 17, 2016, p. 174302. https://doi.org/10.1063/1.4947590.

[56] Dunn, S. M., and Anderson, J. B., "Direct Monte Carlo simulation of chemical reaction systems: Internal energy transfer and an energy-dependent unimolecular reaction," *The Journal of Chemical Physics*, Vol. 99, No. 9, 1993, pp. 6607–6612. https://doi.org/10.1063/1.466185.

[57] Mertz, H., "Modélisation des réactions chimiques dans un code de simulation par la méthode Monte Carlo," Ph.D. thesis, Université Paris-Saclay, 2019. URL https://tel.archives-ouvertes.fr/tel-02110304/file/77248_MERTZ_2019_archivage.pdf.

[58] Scanlon, T. J., White, C., Borg, M. K., Palharini, R. C., Farbar, E., Boyd, I. D., Reese, J. M., and Brown, R. E., "Open-source Direct simulation Monte Carlo chemistry modeling for hypersonic flows," *AIAA Journal*, Vol. 53, No. 6, 2015, pp. 1670–1680. https://doi.org/10.2514/1.J053370.

[59] Liechty, D. S., "Extension of a kinetic approach to chemical reactions to electronic energy levels and reactions involving charged species with application to DSMC simulations," Ph.D. thesis, University of Maryland, 2013.

[60] McQuarrie, D. A., *Statistical thermodynamics*, HarperCollins Publishers, 1973.

[61] Schaerer, R. P., and Torrilhon, M., "The 35-moment system with the maximum-entropy closure for rarefied gas flows," *European Journal of Mechanics-B/Fluids*, Vol. 64, 2017, pp. 30–40. https://doi.org/10.1016/j.euromechflu.2017.01.003.

[62] Jiang, Z., Zhao, W., Chen, W., and Agarwal, R. K., "An undecomposed hybrid algorithm for nonlinear coupled constitutive relations of rarefied gas dynamics," *Commun. Comput. Phys*, Vol. 26, No. 3, 2019, p. 880. https://doi.org/10.4208/cicp.OA-2018-0056.

[63] White, C., "Benchmarking, development and applications of an open source DSMC solver," Ph.D. thesis, University of Strathclyde, 2013.

[64] Bird, G. A., "Sophisticated DSMC," *Notes prepared for a short course at the DSMC07 meeting, Santa Fe, USA*, 2007.

[65] Eggers, A. J., *One-dimensional flows of an imperfect diatomic gas*, Vol. 959, National Advisory Committee for Aeronautics, 1949.

[66] NACA, A. R. S., "Charts for Compressible Flow," *NACA Report*, Vol. 1135, 1953.

[67] Sciacovelli, L., Passiatore, D., Cinnella, P., and Pascazio, G., "Assessment of a high-order shock-capturing central-difference scheme for hypersonic turbulent flow simulations," *arXiv preprint*, 2021. https://doi.org/https://arxiv.org/abs/2103.16426.

[68] Passiatore, D., Sciacovelli, L., Cinnella, P., and Pascazio, G., "Finite-rate chemistry effects in turbulent hypersonic boundary layers: A direct numerical simulation study," *Physical Review Fluids*, Vol. 6, No. 5, 2021, p. 054604. https://doi.org/10.1103/PhysRevFluids.6.054604.

[69] Jaffe, R., "The calculation of high-temperature equilibrium and nonequilibrium specific heat data for N_2, O_2 and NO," *22nd Thermophysics Conference*, 1987, p. 1633. https://doi.org/10.2514/6.1987-1633.

[70] Valentini, P., Norman, P., Zhang, C., and Schwartzentruber, T. E., "Rovibrational coupling in molecular nitrogen at high temperature: An atomic-level study," *Physics of Fluids*, Vol. 26, No. 5, 2014, p. 056103. https://doi.org/10.1063/1.4875279.

[71] Bird, G. A., "Definition of mean free path for real gases," *The Physics of fluids*, Vol. 26, No. 11, 1983, pp. 3222–3223. https://doi.org/10.1063/1.864095.